

Convexification and experimental data for a 3D inverse scattering problem with the moving point source

Vo Anh Khoa^a, Grant W. Bidney^b, Michael V. Klibanov^{a,*}, Loc H. Nguyen^a, Lam H. Nguyen^c, Anders J. Sullivan^c, Vasily N. Astratov^b

^a*Department of Mathematics and Statistics, University of North Carolina at Charlotte, Charlotte, North Carolina 28223, USA.*

^b*Department of Physics and Optical Science, University of North Carolina at Charlotte, Charlotte, NC 28223, USA.*

^c*U.S. Army Research Laboratory, Adelphi, Maryland 20783-1197, USA.*

Abstract

Inverse scattering problems of the reconstructions of physical properties of a medium from boundary measurements are substantially challenging ones. This work aims to verify the performance on experimental data of a newly developed convexification method for a 3D coefficient inverse problem for the case of objects buried in a sandbox a fixed frequency and the point source moving along an interval of a straight line. Using a special Fourier basis, the method of this work strongly relies on a new derivation of a boundary value problem for a system of coupled quasilinear elliptic equations. This problem, in turn is solved via the minimization of a Tikhonov-like functional weighted by a Carleman Weight Function. The global convergence of the numerical procedure is established analytically. The numerical verification is performed using experimental data, which are raw backscatter data of the electric field. These data were collected using a microwave scattering facility at The University of North Carolina at Charlotte.

Keywords: Coefficient inverse problem, multiple point sources, experimental data, Carleman weight, global convergence, Fourier series

2008 MSC: 78A46, 65L70, 65C20

1. Introduction

Inverse and ill-posed problems are ubiquitous in many branches of physical, biological, ecological and social sciences. The goal of this paper is to figure out how to reconstruct physical properties of objects buried closely under the ground on a small depth not exceeding 10 centimeters. Since these objects are buried, then they present a significant challenge in detection and identification of suspicious explosive-like targets (antipersonnel land mines and improvised explosive devices) in military applications. Mathematically, the challenge in solving such problems is the limitation of observable quantities of inputs to the physical-based mathematical systems. In this 3D scenario, only data on a single surface are physically measured in a fixed and specific discrete setting. Certainly, it is expensive and time-consuming to try finer refinements of spatial measurements of observable quantities.

^{*}The work of Khoa, Bidney, Klibanov, L. H. Nguyen and Astratov was supported by US Army Research Laboratory and US Army Research Office grant W911NF-19-1-0044. The work of Khoa was also partly supported by the Research Foundation-Flanders (FWO) under the project named “Approximations for forward and inverse reaction-diffusion problem related to cancer models”.

*Corresponding author.

Email addresses: vakhao.hcmus@gmail.com (Vo Anh Khoa), gbidney@uncc.edu (Grant W. Bidney), mklibanv@uncc.edu (Michael V. Klibanov), loc.nguyen@uncc.edu (Loc H. Nguyen), lam.h.nguyen2.civ@mail.mil (Lam H. Nguyen), anders.j.sullivan.civ@mail.mil (Anders J. Sullivan), astratov@uncc.edu (Vasily N. Astratov)

We call a numerical method for a nonlinear ill-posed problem *globally convergent* if there is a theorem which guarantees that this method delivers at least one point in a sufficiently small neighborhood of the exact solution without any advanced knowledge of this neighborhood. In other words, this theorem guarantees that although a good first guess for the solution is not required, still a good approximation for the solution will be obtained by that numerical method. The convexification method we work here is a globally convergent one.

1.1. *Scopes and novelty*

The goal here is to solve a 3D Coefficient Inverse Problem (CIP) for the case of the experimentally collected backscattering data. In doing so, we want to estimate the dielectric constants and shapes of buried targets. We consider here the case when the point source moves along an interval of a straight line and the frequency is fixed. In this work, we apply the globally convergent convexification method, which has been developed by the third author and his coauthors for a significant number of years. On the other hand, a large amount of previous papers concerning the convexification with numerical investigations consider the scenario when either the point source or the direction of the incident plane wave is fixed and the frequency is varied; cf. [27, 28, 29, 30, 31, 32, 46]. While locations and dielectric constants of targets are imaged accurately in such cases, shapes of targets are not accurately imaged; see, e.g., images of [30] for the case of experimentally collected data.

Thus, the idea here is to move the source in a hope that this would provide better images of shapes of targets of interest while still preserving accurate values of computed dielectric constants. This novel insight was first implemented in [17], where it was shown that it works well for computationally simulated backscattering data: both dielectric constants and shapes of targets were accurately imaged via a new version of the convexification method. In this paper, we continue to verify the computational performance of the idea of [17] using experimental backscattering data. These data are raw backscatter data of the electric field that we collected using a microwave scattering facility at our University. We then show here that the version of [17] the convexification method accurately computes values of dielectric constants as well as shapes of targets buried in a sandbox (including those with even rather complicated shapes). Notice that since the frequency is fixed both in [17] and here, then the data we use are non overdetermined ones.

We realize that estimates of dielectric constants, shapes and locations of buried targets mimicking explosives are insufficient to distinguish between explosives and non-explosives. Nevertheless, these estimates might serve in the future as a piece of the information, which is an additional one to the features currently used for classifications of explosive-like targets. Hence, this new information might help to decrease the false alarm rate.

The convexification method “convexifies” a weighted Tikhonov-like functional via using a suitable Carleman Weight Function (CWF). While starting from the first inception in 1981 (cf. [11]) with the only goal at that time of proofs of global uniqueness theorems for CIPs (also, see, e.g., [8, 21, 47]), the notion of applications of Carleman estimates to CIPs got a new aspect nowadays in terms of numerical methods for CIPs. This is because, driven by the CWF, the resulting convexified cost functionals avoid being trapped in local minima and ravines.

The first publications on the convexification were in 1995 and 1997; cf. [18, 19]. Also, the reader can be referred to some other initial follow-up results in [9, 20, 22]. However, these past papers were purely theoretical ones. The reason was that some important mathematical facts leading to numerical implementations were unknown at that time, although some numerical results were published in [20]. In 2017, the work [3] has clarified those facts. This led to a significant number of recent publications on the convexification, where both analytical and numerical results were present; cf. [17, 27, 28, 29, 30, 31, 32, 46]. It is worth mentioning that papers [27, 28, 30] address the performance of the convexification on experimental data, which is the same research line of this article. In particular, the paper [30] considers

experimental data for buried objects for the case of a single location of the point source and multiple frequencies.

In our four latest publications [29, 30, 31, 32] the convexification method is based upon the derivation of boundary value problem with overdetermined boundary conditions for a system of coupled elliptic PDEs. In fact, some of those boundary conditions are Cauchy data. Next, an approximate solution of this system is found via the minimization of a weighted globally strictly convex Tikhonov-like functional with a CWF in it. In the case of CIPs for the Helmholtz equation considered in [29, 30], multiple frequencies were used and only a single location of the point source.

The boundary value problem mentioned in the previous paragraph is about finding spatially dependent coefficients of a certain truncated Fourier series with respect to a new orthonormal basis in the L^2 space, which was first introduced in [26]. In [17], the theory of that version of the convexification was developed for the continuous case. Unlike [17], we consider here a “partial finite difference” case, which is another novelty of this article. This means that partial derivatives with respect to two out of three variables are written in finite differences. However, we do not allow the grid step size to tend to zero. This agrees with the fact that it is certainly expensive in real-world applications to decrease the grid step size indefinitely. We point out that an important advantage of using partial finite differences is that we do not use the regularization penalty term in the weighted Tikhonov-like functional. The global convergence analysis in the framework of partial finite differences is performed here. We believe that this is a significant analytical novelty of our work.

1.2. Related works and outline of the paper

The existing literature on this topic is huge to be singled out. Conventional numerical approaches to CIPs rely on the minimization of some least squares Tikhonov functionals; see, e.g., [12, 13, 14]. It is well known, however, that these functionals are non convex and typically have multiple local minima and ravines. Thus, convergence of a minimization procedure to the exact solution can be sometimes guaranteed in such a case only if its starting point is located in a sufficiently small neighborhood of that solution, i.e. this would be a *locally* convergent numerical method. Unlike this, the concept of the convexification leads to globally convergent numerical methods.

We now refer only to the closest publications, since this paper is not a survey. A version of the convexification, which is different from ours (see above-cited references), has been developed by Baudouin, de Buhan, Ervedoza and Osses (cf. [6, 7]) for two CIPs for the hyperbolic equations and then for quasilinear parabolic equations (cf. Boulakia, de Buhan and Schwindt [10] and Le and Nguyen [36]). In this version, a CWF is used to construct a sort of a contractual mapping operator. A nice feature of these techniques is that the corresponding numerical method converge globally, which again accentuates the importance of the inclusion of CWFs in numerical schemes. The publications [6, 7, 10] work within the framework of the Bukhgeim–Klibanov method (cf. [8, 11, 20, 21]), which assumes that an initial condition is not vanishing in the entire domain of interest. On the other hand, all our above cited publications about the convexification for the CIPs for the wave propagation processes essentially work with the case when the forward problem for the Helmholtz equation can be reduced via the Fourier transform to the one for a hyperbolic equation, in which one of initial conditions is identical to zero and the second one is the δ -function (also see [32] for a similar situation in the time domain case).

CIPs for the fixed frequency case have been extensively studied by Novikov and his coauthors since 1988; cf. [39]. In particular, several reconstruction methods were proposed by this group and numerical results were also accompanied in [1, 2, 40, 41]. It is worth noting that these CIPs and reconstruction techniques are different from the ones we are using. A nice feature of these reconstruction methods is that they are in the category of globally convergent numerical methods, since they do not require a good first guess; see the second paragraph of this section for the definition of the global convergence. An interesting feature of [1, 41] is that these publications consider the case of non overdetermined data for

the reconstruction of the potential of the Schrödinger equation at high values of the wavenumber are considered in [1, 41]. Furthermore, the data in [1] are phaseless. Corresponding numerical results of this series of works are published in [1, 2].

There is another feature of the techniques of the Novikov's group, which is philosophically close to one of features of our technique. Their reconstruction procedures rely on certain steps on truncations of Fourier series. On the other hand, we also truncate the Fourier series in this work; see Remark 4. And also, neither we nor the group of Novikov cannot prove convergence as the truncation number $N \rightarrow \infty$.

Recently, Bakushinsky and Leonov have proposed an algorithm for solving a CIP with multi frequency data; cf. [4]. Their method is based on the solution of an integral equation of the first kind generated by the fundamental solution of the Helmholtz equation in a homogeneous medium. In the case of the time dependent data and low contrast targets, we refer to Goncharsky and Romanov [13] for computationally simulated data and to Goncharsky, Romanov and Seryozhnikov [14] for a quite successful application of the method of [13] to experimental data.

This paper is organized as follows. Section 2 is devoted to the mathematical statement of the forward and inverse problems. In section 3, we present the derivation of the quasi-linear PDE system and then design a weighted Tikhonov-like functional that we want to minimize in the numerical process. Thereby, an important part in this section will be principal proofs of convergence of the minimizer towards the true solution in a finite difference framework. In section 4, we delineate our numerical results with experimental data. Here, the so-called data propagation procedure is revisited.

2. Statement of the problem

Let $\mathbf{x} = (x, y, z) \in \mathbb{R}^3$. Consider a rectangular prism $\Omega = (-R, R) \times (-R, R) \times (-b, b)$ in \mathbb{R}^3 for $R, b > 0$ as our computational domain of interest. Let $c(\mathbf{x})$ be a spatially distributed dielectric constant of the medium. We assume that the function $c(\mathbf{x})$ is smooth and also that

$$\begin{cases} c(\mathbf{x}) \geq 1 & \text{in } \mathbb{R}^3, \\ c(\mathbf{x}) = 1 & \text{in } \mathbb{R}^3 \setminus \Omega. \end{cases} \quad (1)$$

The second line of (1) means that we are assuming to have vacuum outside the domain of interest Ω . Let the number $d > b$ and let $a_1 < a_2$. We consider a line of sources

$$L_{\text{src}} := \{(\alpha, 0, -d) : a_1 \leq \alpha \leq a_2\},$$

which is parallel to the x -axis and is located outside of the closed domain $\overline{\Omega}$. The distance from L_{src} to the xy -plane is d , and the length of the line of sources is $(a_2 - a_1)$. Using this setting, for each $\alpha \in [a_1, a_2]$ we arrange the point source $\mathbf{x}_\alpha := (\alpha, 0, -d)$ located on the straight line L_{src} . We also define the near-field measurement site as the lower side of the prism Ω ,

$$\Gamma := \{\mathbf{x} : |x|, |y| < R, z = -b\}.$$

Throughout the paper, we use either α or \mathbf{x}_α to indicate the dependence of a function/parameter/number on those point sources. We denote by u , u_i and u_s the total wave, incident wave and scattered wave, respectively. Also, we note that $u = u_i + u_s$.

Forward problem

Given the wavenumber $k > 0$ and the function $c(\mathbf{x})$, the forward problem is to seek the function $u(\mathbf{x}, \alpha)|_\Gamma$ such that $u = u(\mathbf{x}, \alpha)$ satisfying the Helmholtz equation with the radiation boundary condition,

which reads as

$$\Delta u + k^2 c(\mathbf{x}) u = -\delta(\mathbf{x} - \mathbf{x}_\alpha) \quad \text{in } \mathbb{R}^3, \quad (2)$$

$$\lim_{r \rightarrow \infty} r (\partial_r u - iku) = 0 \quad \text{for } r = |\mathbf{x} - \mathbf{x}_\alpha|, i = \sqrt{-1}. \quad (3)$$

Here, the incident wave is

$$u_i(\mathbf{x}, \alpha) = \frac{\exp(ik|\mathbf{x} - \mathbf{x}_\alpha|)}{4\pi|\mathbf{x} - \mathbf{x}_\alpha|}. \quad (4)$$

Moreover, we can deduce that the scattered wave satisfies the integral equation:

$$\begin{aligned} u_s(\mathbf{x}, \alpha) &= k^2 \int_{\mathbb{R}^3} \frac{\exp(ik|\mathbf{x} - \mathbf{x}'|)}{4\pi|\mathbf{x} - \mathbf{x}'|} (c(\mathbf{x}') - 1) u(\mathbf{x}', \alpha) d\mathbf{x}' \\ &= k^2 \int_{\Omega} \frac{\exp(ik|\mathbf{x} - \mathbf{x}'|)}{4\pi|\mathbf{x} - \mathbf{x}'|} (c(\mathbf{x}') - 1) u(\mathbf{x}', \alpha) d\mathbf{x}', \quad \mathbf{x} \in \mathbb{R}^3, \end{aligned} \quad (5)$$

since $c - 1$ is compactly supported in Ω ; see again (1). Combining (4) and (5), we find that the total wave u satisfies the Lippmann–Schwinger equation:

$$u(\mathbf{x}, \alpha) = u_i(\mathbf{x}, \alpha) + k^2 \int_{\Omega} \frac{\exp(ik|\mathbf{x} - \mathbf{x}'|)}{4\pi|\mathbf{x} - \mathbf{x}'|} (c(\mathbf{x}') - 1) u(\mathbf{x}', \alpha) d\mathbf{x}', \quad \mathbf{x} \in \mathbb{R}^3.$$

Remark 1. Even though the propagation of the electromagnetic wave field is governed by the system of the Maxwell equations, we model our process by the single Helmholtz equation. The reason is twofold. First, it was demonstrated numerically in Appendix for [33] that if the incident electric wave field $E = (E_x, E_y, E_z)$ has only one non zero component, then the propagation of this component in a heterogeneous medium is governed equally well by the Helmholtz equation and the Maxwell equations. This is true for at least a rather simply structured medium. Second, both our previous [8, 30, 37, 44] and current results for experimental data demonstrate a good reconstruction accuracy for the case of modeling by the Helmholtz equation.

Remark 2. Physically, $u(\mathbf{x}, \alpha)$ is such a component of the electric field $E = (E_x, E_y, E_z)$ which was non zero when being incident, whereas other two components of the incident electric field E equal zero. As it was mentioned in Remark 1, the propagation of this component in a heterogeneous medium is governed equally well by the Helmholtz equation and the full system of Maxwell's equations, as it was shown numerically in Appendix for [33]. In the particular case of our experimental data, $u = E_y$ is indicated.

Coefficient inverse problem

Given $k > 0$, the *inverse problem* is to reconstruct the smooth dielectric constant $c(\mathbf{x})$, $\mathbf{x} \in \Omega$ satisfying conditions (1) from the boundary measurement as near-field data

$$F(\mathbf{x}, \mathbf{x}_\alpha) = u(\mathbf{x}, \alpha) \quad \text{for } \mathbf{x} \in \Gamma, \mathbf{x}_\alpha \in L_{\text{src}}, \quad (6)$$

where $u(\mathbf{x}, \alpha)$ is the total wave associated to the incident wave u_i of (4). A schematic diagram of locations of sources and detectors is presented on Figure 1b in subsection 4.1.

Currently uniqueness theorem for this CIP can be proven only in the case when the right hand side of equation (2) is not vanishing in $\bar{\Omega}$. Such a theorem can be proven by the method of [11] which was mentioned in the Introduction. In addition, uniqueness can be proven if working within an approximate mathematical model. In this regard, uniqueness follows from Theorem 3.2 of [17], and, for the approximate mathematical model of this paper, it follows from Theorem 4.

3. A globally convergent numerical method

3.1. Derivation of a system of coupled quasilinear elliptic PDEs

Since our line of sources L_{src} is located outside of $\bar{\Omega}$, we deduce this system from the Helmholtz homogeneous version of equation (2) and for each $\alpha \in [a_1, a_2]$

$$\Delta u + k^2 c(\mathbf{x}) u = 0 \quad \text{in } \Omega. \quad (7)$$

Now, we set that

$$\log u_i(\mathbf{x}, \alpha) = ik |\mathbf{x} - \mathbf{x}_\alpha| - \log(4\pi |\mathbf{x} - \mathbf{x}_\alpha|),$$

which then leads to

$$\nabla(\log u_i(\mathbf{x}, \alpha)) = \frac{ik(\mathbf{x} - \mathbf{x}_\alpha)}{|\mathbf{x} - \mathbf{x}_\alpha|} - \frac{\mathbf{x} - \mathbf{x}_\alpha}{|\mathbf{x} - \mathbf{x}_\alpha|^2}. \quad (8)$$

Even though we work with a fixed value of k , we now temporarily indicate the dependence of the function u on k , i.e. $u = u(\mathbf{x}, \alpha, k)$. Using the asymptotic behavior of $u(\mathbf{x}, \alpha, k)$ at $k \rightarrow \infty$ (cf. [25]), one can prove, similarly with [25], that there exists a sufficiently large number $\bar{k} > 0$ such that $u(\mathbf{x}, \alpha, k) \neq 0$ for $k \geq \bar{k}$, $\mathbf{x} \in \bar{\Omega}$, $\alpha \in [a_1, a_2]$. Furthermore, it was shown in [29, 30] that, using that asymptotic behavior, one can uniquely define the function $\log u(\mathbf{x}, \alpha, k)$ for $k \geq \bar{k}$, $\mathbf{x} \in \bar{\Omega}$, $\alpha \in [a_1, a_2]$. Thus, we assume below that our specific value of the wave number $k = k_0$ we work with is sufficiently large, $k_0 \geq \bar{k}$, and also that the function $\log u(\mathbf{x}, \alpha, k_0)$ is uniquely defined as in [29, 30]. In particular, we work with the dimensionless values $k_0 \geq 6.62$; see subsection 4.5. We point out that since we work below only with the derivatives (with respect to \mathbf{x} and α) of $\log u(\mathbf{x}, \alpha, k_0)$, i.e.

$$\begin{aligned} \nabla(\log u(\mathbf{x}, \alpha, k_0)) &:= \nabla_{\mathbf{x}}(\log u(\mathbf{x}, \alpha, k_0)) = \nabla_{\mathbf{x}} u(\mathbf{x}, \alpha, k_0) / u(\mathbf{x}, \alpha, k_0), \\ \Delta(\log u(\mathbf{x}, \alpha, k_0)) &:= \Delta_{\mathbf{x}}(\log u(\mathbf{x}, \alpha, k_0)), \\ \partial_\alpha(\nabla(\log u(\mathbf{x}, \alpha, k_0))) &:= \partial_\alpha(\nabla_{\mathbf{x}}(\log u(\mathbf{x}, \alpha, k_0))), \\ \partial_\alpha(\Delta(\log u(\mathbf{x}, \alpha, k_0))) &:= \partial_\alpha(\Delta_{\mathbf{x}}(\log u(\mathbf{x}, \alpha, k_0))), \end{aligned}$$

then what we actually need in our work is not that definition of $\log u(\mathbf{x}, \alpha, k_0)$ but rather that $u(\mathbf{x}, \alpha, k_0) \neq 0$. However, we have not noticed in our computations those values of $|u(\mathbf{x}, \alpha, k_0)|$ which would be close to zero.

Denote $v_0(\mathbf{x}, \alpha) = u(\mathbf{x}, \alpha) / u_i(\mathbf{x}, \alpha)$. We define the function $v(\mathbf{x}, \alpha)$ as

$$v(\mathbf{x}, \alpha) := \log(v_0(\mathbf{x}, \alpha)) = \log(u(\mathbf{x}, \alpha)) - \log(u_i(\mathbf{x}, \alpha)) \quad \text{for } \mathbf{x} \in \Omega, \alpha \in [a_1, a_2].$$

Hence, one computes that

$$\nabla v(\mathbf{x}, \alpha) = \frac{\nabla v_0(\mathbf{x}, \alpha)}{v_0(\mathbf{x}, \alpha)}, \quad \Delta v(\mathbf{x}, \alpha) = \frac{\Delta v_0(\mathbf{x}, \alpha)}{v_0(\mathbf{x}, \alpha)} - \left(\frac{\nabla v_0(\mathbf{x}, \alpha)}{v_0(\mathbf{x}, \alpha)} \right)^2. \quad (9)$$

Thus, using (7)–(9) we derive the equation for v ,

$$\Delta v + (\nabla v)^2 + 2\nabla v \cdot \nabla(\log(u_i(\mathbf{x}, \alpha))) = -k^2(c(\mathbf{x}) - 1) \quad \text{for } \mathbf{x} \in \Omega. \quad (10)$$

Remark 3. Observe that if the function $v(\mathbf{x}, \alpha)$ is known, then we can immediately find the target coefficient $c(\mathbf{x})$ via equation (10).

We now differentiate (10) with respect to α and use (8) to obtain the following third-order PDE:

$$\Delta \partial_\alpha v + 2\nabla v \cdot \nabla \partial_\alpha v + 2\nabla \partial_\alpha v \cdot \left[\frac{ik(\mathbf{x} - \mathbf{x}_\alpha)}{|\mathbf{x} - \mathbf{x}_\alpha|} - \frac{\mathbf{x} - \mathbf{x}_\alpha}{|\mathbf{x} - \mathbf{x}_\alpha|^2} \right] + 2\partial_\alpha \left[\frac{ik(\mathbf{x} - \mathbf{x}_\alpha)}{|\mathbf{x} - \mathbf{x}_\alpha|} - \frac{\mathbf{x} - \mathbf{x}_\alpha}{|\mathbf{x} - \mathbf{x}_\alpha|^2} \right] \cdot \nabla v = 0.$$

To simplify the presentation, this equation can be rewritten as:

$$\Delta \partial_\alpha v + 2\nabla v \cdot \nabla \partial_\alpha v + 2\nabla \partial_\alpha v \cdot \tilde{\mathbf{x}}_\alpha + 2\hat{\mathbf{x}}_\alpha \cdot \nabla v = 0 \quad \text{for } \mathbf{x} \in \Omega, \quad (11)$$

where, for $\mathbf{x} - \mathbf{x}_\alpha = (x - \alpha, y, z + d) \in \mathbb{R}^3$,

$$\begin{aligned} \tilde{\mathbf{x}}_\alpha &= \frac{ik(\mathbf{x} - \mathbf{x}_\alpha)}{|\mathbf{x} - \mathbf{x}_\alpha|} - \frac{\mathbf{x} - \mathbf{x}_\alpha}{|\mathbf{x} - \mathbf{x}_\alpha|^2}, \\ \hat{\mathbf{x}}_\alpha &= \frac{ik}{|\mathbf{x} - \mathbf{x}_\alpha|^3} \left(-y^2 - (z + d)^2, (x - \alpha)y, (x - \alpha)z \right) \\ &\quad - \frac{1}{|\mathbf{x} - \mathbf{x}_\alpha|^4} \left((x - \alpha)^2 - y^2 - (z + d)^2, 2(x - \alpha)y, 2(x - \alpha)z \right). \end{aligned}$$

Even though the unknown coefficient $c(\mathbf{x})$ is not present in equation (11) for the function $v(\mathbf{x}, \alpha)$, it is still not easy to solve the nonlinear third-order PDE (11). To circumvent this, we rely on a special orthonormal basis with respect to α to turn (11) into a system of coupled quasilinear elliptic PDEs.

For $\alpha \in (a_1, a_2)$, let $\{\Psi_n(\alpha)\}_{n=0}^\infty$ be the special orthonormal basis in $L^2(a_1, a_2)$, which was first proposed in [26]. Herewith, the construction of this basis is shortly revisited. For each $n \in \mathbb{N}$, let $\varphi_n(\alpha) = \alpha^n e^\alpha$ for $\alpha \in [a_1, a_2]$. The set $\{\varphi_n(\alpha)\}_{n=0}^\infty$ is linearly independent and complete in $L^2(a_1, a_2)$. Using the Gram–Schmidt orthonormalization procedure, we can obtain the orthonormal basis $\{\Psi_n(\alpha)\}_{n=0}^\infty$ in $L^2(a_1, a_2)$, which possesses the following special properties:

- $\Psi_n \in C^\infty[a_1, a_2]$ for all $n \in \mathbb{N}$;
- Let $s_{mn} = \langle \Psi'_n, \Psi_m \rangle$, where $\langle \cdot, \cdot \rangle$ denotes the scalar product in $L^2(a_1, a_2)$. Then the square matrix $S_N = (s_{mn})_{m,n=0}^{N-1}$ for $N \in \mathbb{N}^*$ is invertible in the sense that

$$s_{mn} = \begin{cases} 1 & \text{if } n = m, \\ 0 & \text{if } n < m. \end{cases}$$

We note that even though the Gram–Schmidt procedure is unstable if using the infinite number of functions $\varphi_n(\alpha)$, we have observed numerically that it has good stability properties for rather small numbers N which we use. Neither classical orthogonal polynomials nor the classical basis of trigonometric functions do not hold the second property. The matrix S_N is an upper diagonal matrix with $\det(S_N) = 1$. On the other hand, the special second property allows us to reduce the third-order PDE (11) to a system of coupled elliptic PDEs.

Given $N \in \mathbb{N}^*$, we consider the following truncated Fourier series for v :

$$v(\mathbf{x}, \alpha) = \sum_{n=0}^{N-1} \langle v(\mathbf{x}, \cdot), \Psi_n(\cdot) \rangle \Psi_n(\alpha) \quad \text{for } \mathbf{x} \in \Omega, \alpha \in [a_1, a_2]. \quad (12)$$

Substitution (12) into (11) gives

$$\begin{aligned} &\sum_{n=0}^{N-1} \Psi'_n(\alpha) \Delta v_n(\mathbf{x}) + 2 \sum_{n=0}^{N-1} \sum_{l=0}^{N-1} \Psi_n(\alpha) \Psi'_l(\alpha) \nabla v_n(\mathbf{x}) \cdot \nabla v_l(\mathbf{x}) \\ &+ 2 \sum_{n=0}^{N-1} \Psi'_n(\alpha) \nabla v_n(\mathbf{x}) \cdot \tilde{\mathbf{x}}_\alpha + 2 \sum_{n=0}^{N-1} \Psi_n(\alpha) \hat{\mathbf{x}}_\alpha \cdot \nabla v_n(\mathbf{x}) = 0. \end{aligned} \quad (13)$$

Multiplying both sides of (13) by $\Psi_m(\alpha)$ for $0 \leq m \leq N-1$ and then integrating the resulting equation with respect to α , we obtain the following system of coupled elliptic equations:

$$\Delta V(\mathbf{x}) + K(\nabla V(\mathbf{x})) = 0 \quad \text{for } \mathbf{x} \in \Omega, \quad (14)$$

$$\nabla V(\mathbf{x}) \cdot \mathbf{n} = 0 \quad \text{for } \mathbf{x} \in \partial\Omega \setminus \Gamma, \quad (15)$$

$$V(\mathbf{x}) = \psi_0(\mathbf{x}), V_z(\mathbf{x}) = \psi_1(\mathbf{x}) \quad \text{for } \mathbf{x} \in \Gamma. \quad (16)$$

Here, $V(\mathbf{x}) \in \mathbb{R}^N$ is the unknown vector function given by

$$V(\mathbf{x}) = (v_0(\mathbf{x}) \quad v_1(\mathbf{x}) \quad \cdots \quad v_{N-1}(\mathbf{x}))^T. \quad (17)$$

Thus, we have obtained a boundary value problem (14)–(16) for a system of coupled quasilinear elliptic PDEs (14). Boundary conditions (16) are overdetermined ones. Note that conditions (16) are the Cauchy data. A Lipschitz stability estimate for problem (14)–(16) is obtained in [17].

In PDE (14), we denote by $K(\nabla V(\mathbf{x})) = S_N^{-1} f(\nabla V(\mathbf{x}))$, where $f = \left((f_m)_{m=0}^{N-1} \right)^T \in \mathbb{R}^N$ is quadratic with respect to the first derivative of components of $V(\mathbf{x})$,

$$\begin{aligned} f_m(\nabla V(\mathbf{x})) &= 2 \sum_{n,l=0}^{N-1} \nabla v_n(\mathbf{x}) \cdot \nabla v_l(\mathbf{x}) \int_{a_1}^{a_2} \Psi_m(\alpha) \Psi_n(\alpha) \Psi'_l(\alpha) d\alpha \\ &+ 2 \sum_{n=0}^{N-1} \int_{a_1}^{a_2} \Psi_m(\alpha) \Psi'_n(\alpha) \nabla v_n(\mathbf{x}) \cdot \tilde{\mathbf{x}}_\alpha d\alpha + 2 \sum_{n=0}^{N-1} \int_{a_1}^{a_2} \Psi_m(\alpha) \Psi_n(\alpha) \hat{\mathbf{x}}_\alpha \cdot \nabla v_n(\mathbf{x}) d\alpha. \end{aligned} \quad (18)$$

Now, we explain how to obtain the Cauchy data (16). First, an obvious application of the expansion (12) to the near-field data (6) gives us the function ψ_0 at Γ . However, our experimental data are in fact far-field type; see section 4. This means that we collect the experimental data far from the domain of interest, i.e. on the plane $\{z = -D\}$ for $D > b$. However, the far-field data do not look nice as we experienced in many previous works; cf. e.g. [37]. Therefore, we rely on the so-called “data propagation technique” to get the data closer to the target’s side and to reduce the size of the domain of interest Ω we are considering. In our work, this technique is revisited in subsection 4.4. As a by-product of this technique, we can obtain an approximation of the z -derivative of the function u at the near-field measurement site Γ . This leads to the presence of the function ψ_1 in (16).

We now explain the Neumann zero boundary condition (15) on $\partial\Omega \setminus \Gamma$. Assuming that, due to the radiation condition (3), $(\partial_n u - iku)(\mathbf{x}, \alpha)|_{\partial\Omega \setminus \Gamma} \approx 0$ and also that $(\partial_n u_i - iku_i)|_{\partial\Omega \setminus \Gamma} \approx 0$, we easily obtain $\partial_n v(\mathbf{x}, \alpha)|_{\partial\Omega \setminus \Gamma} \approx 0$ for $v(\mathbf{x}, \alpha) = \log(u(\mathbf{x}, \alpha)/u_i(\mathbf{x}, \alpha))$. Hence, condition (15) follows from the latter and is an approximate one.

Remark 4. Using the truncated Fourier series (12), we actually replace the original CIP with its approximation. Thus, we work with an approximate mathematical model. Substantial difficulties in solving our CIP are linked with both its nonlinearity and ill-posedness. Due to these difficulties, we cannot prove convergence at $N \rightarrow \infty$, where N is the number of Fourier coefficients in that truncated Fourier series. Besides, we recall that another feature of our approximate mathematical model is that we do not allow the grid step size of our partial finite differences to tend to zero. We believe that good reconstruction results, which we demonstrate below, justify our approximate mathematical model. It is worthy to mention here that it is quite **typical** in the field of CIPs to consider approximate mathematical models caused by truncations of certain Fourier series without proofs of convergence at $N \rightarrow \infty$. In such cases good numerical results serve as justifications of these models. In this regard we refer to works [1, 2, 15, 16, 40, 41]. More detailed discussions of the issue of approximate mathematical models can be found in [17, 32].

3.2. A weighted cost functional

We set

$$L(V)(\mathbf{x}) = \Delta V(\mathbf{x}) + K(\nabla V(\mathbf{x})). \quad (19)$$

We use partial finite difference setting via considering finite differences with respect to x, y and keeping the standard derivatives with respect to z . In this setting, we look for an approximate solution of the system (14)–(16) using the minimization of a Tikhonov-type functional weighted by a suitable Carleman Weight Function (CWF).

Let the numbers $\theta > b$ and $\lambda \geq 1$. We define our CWF as

$$\mu_\lambda(z) = \exp\left(2\lambda(z - \theta)^2\right) \quad \text{for } z \in [-b, b]. \quad (20)$$

The choice $\theta > b$ is based on the fact that the gradient of the CWF should not vanish in the closed domain $\bar{\Omega}$. Observe that the CWF is decreasing for $z \in (-b, b)$ and

$$\max_{z \in [-b, b]} \mu_\lambda(z) = \mu_\lambda(-b) = e^{2\lambda(b+\theta)^2}, \quad (21)$$

$$\min_{z \in [-b, b]} \mu_\lambda(z) = \mu_\lambda(b) = e^{2\lambda(b-\theta)^2}. \quad (22)$$

This means that the CWF (20) attains its maximal value on the measurement site Γ , and it attains its minimal value on the opposite side. This notion of using the CWF is essential because it “maximizes” the influence of the actual measured boundary data at $z = -b$. Furthermore, the CWF plays the vital role in convexifying the cost functional globally in both this and other types of the convexification method. In fact what the CWF does is that it controls the nonlinear term. In our particular case this term is $K(\nabla V(\mathbf{x}))$ in (14).

3.2.1. Preliminaries of the partial finite differences setting

We use the same grid step size h in x and y directions. Introduce two partitions of the closed interval $[-R, R]$,

$$\begin{aligned} -R &= x_0 < x_1 < \dots < x_{Z_h-1} < x_{Z_h} = R, & x_p - x_{p-1} &= h, \\ -R &= y_0 < y_1 < \dots < y_{Z_h-1} < y_{Z_h} = R, & y_q - y_{q-1} &= h. \end{aligned}$$

We write the differential operator in (19) in the following partial finite difference form. For any N -dimensional vector function $u(\mathbf{x})$, we denote by $u_{p,q}^h(z) = u(x_p, y_q, z)$ the corresponding semi-discrete function defined at grid points $\{(x_p, y_q)\}_{p,q=0}^{Z_h}$. Thus, the interior grid points are $\{(x_p, y_q)\}_{p,q=1}^{Z_h-1}$. Denote

$$\Omega_h = \left\{ (x_p, y_q, z) : \{(x_p, y_q)\}_{p,q=0}^{Z_h-1} \subset [-R, R] \times [-R, R], z \in (-b, b) \right\},$$

$$\Gamma_h = \left\{ (x_p, y_q, -b) : \{(x_p, y_q)\}_{p,q=0}^{Z_h-1} \subset [-R, R] \times [-R, R] \right\}.$$

Henceforth, the corresponding Laplace operator in the partial finite differences is given by

$$\Delta^h u^h = u_{zz}^h + u_{xx}^h + u_{yy}^h,$$

where, for interior points of Ω_h , we use

$$u_{xx}^h = h^{-2} \left(u_{p+1,q}^h(z) - 2u_{p,q}^h(z) + u_{p-1,q}^h(z) \right), \quad p, q \in [1, Z_h - 1]$$

and similarly for the finite difference operator u_{yy}^h . As to the gradient operator, we write for interior points $\nabla^h u_{p,q}(z) = (\partial_x^h u_{p,q}(z), \partial_y^h u_{p,q}(z), \partial_z u_{p,q}^h(z))$, where

$$\partial_x^h u_{p,q}^h(z) = (2h)^{-1} \left(u_{p+1,q}^h(z) - u_{p-1,q}^h(z) \right).$$

To simplify the presentation, we consider any N -D complex valued function $W = \operatorname{Re} W + i \operatorname{Im} W$ as the $2N$ -D vector function with real valued components $(\operatorname{Re} W, \operatorname{Im} W) := (W_1, W_2) := W \in \mathbb{R}^{2N}$. Also, below for any complex number $a \in \mathbb{C}$ we denote \bar{a} its complex conjugate.

Denote $w^h(z)$ the vector function $w^h(z) = \{w_{p,q}(z)\}_{p,q=0}^{Z_h}$, where $w_{p,q}^h(z) = w(x_p, y_q, z)$. We introduce the Hilbert spaces $H_{2N}^{2,h} = H_{2N}^{2,h}(\Omega_h)$ and $L_{2N}^{2,h} = L_{2N}^{2,h}(\Omega_h)$ of semi-discrete complex valued functions as follows:

$$H_{2N}^{2,h} = \left\{ w^h(z) : \|w^h\|_{H_{2N}^{2,h}}^2 := \sum_{p,q=1}^{Z_h-1} \sum_{m=0}^2 h^2 \int_{-b}^b \left| \partial_z^m w_{p,q}^h(z) \right|^2 dz < \infty \right\},$$

$$L_{2N}^{2,h} = \left\{ w^h(z) : \|w^h\|_{L_{2N}^{2,h}}^2 := \sum_{p,q=1}^{Z_h-1} h^2 \int_{-b}^b \left| w_{p,q}^h(z) \right|^2 dz < \infty \right\}.$$

We also define the subspace $H_{2N,0}^{2,h} \subset H_{2N}^{2,h}$ as

$$H_{2N,0}^{2,h} = \left\{ w^h(z) \in H_{2N}^{2,h} : \nabla^h w_{p,q}^h(z) \Big|_{\partial\Omega_h \setminus \Gamma_h} \cdot \mathbf{n} = 0, w_{p,q}^h(z) \Big|_{\Gamma_h} = \partial_z w_{p,q}^h(z) \Big|_{\Gamma_h} = 0 \right\}.$$

Let $h_0 > 0$ be a fixed positive constant. We assume below that

$$h \geq h_0 > 0. \quad (23)$$

Thus, (23) means that we do not allow the grid step size to tend to zero.

3.2.2. The semi-discrete form of the weighted cost functional and Carleman estimate

Following (17), denote

$$V^h(z) = (v_0^h(z) \quad v_1^h(z) \quad \cdots \quad v_{N-1}^h(z))^T.$$

We now consider the following weighted Tikhonov-like functional $J_\lambda : H_{2N}^{2,h}(\Omega_h) \rightarrow \mathbb{R}_+$,

$$J_{h,\lambda}(V^h) = \sum_{p,q=1}^{Z_h-1} h^2 \int_{-b}^b \left| L^h(V^h(z)) \right|^2 \mu_\lambda(z) dz, \quad (24)$$

where the CWF $\mu_\lambda(z)$ is defined in (20) and $L^h(V^h(z))$ is the operator (19) written in partial finite differences,

$$L^h(V^h(z)) = \Delta^h V^h(z) + K(\nabla^h V^h(z)). \quad (25)$$

Let $M > 0$ be an arbitrary number. We define the set $B(M) \subset H_{2N}^{2,h}(\Omega_h)$ as

$$B(M) := \left\{ V^h \in H_{2N}^{2,h} : \|V^h\|_{H_{2N}^{2,h}} < M, V_{\Gamma_h}^h = \psi_0^h, \partial_z V_{\Gamma_h}^h = \psi_1^h \right\}. \quad (26)$$

The embedding theorem and (23) imply that

$$\overline{B(M)} \subset C_{2N}^{1,h}(\overline{\Omega_h}) \quad \text{and} \quad \|V^h\|_{C_{2N}^{1,h}(\overline{\Omega_h})} \leq C_1 \quad \text{for all } V^h \in \overline{B(M)}. \quad (27)$$

Here the number $C_1 > 0$ depends only on M and h_0 . Since the lower estimate h_0 of our grid step size h is fixed by (23), we neglect below the h -dependence of constants used in proofs of our results.

Minimization problem

This problem is formulated as: *Minimize the cost functional $J_\lambda(V^h)$ on the set $\overline{B(M)}$.*

Below we prove a one-dimensional Carleman estimate. This estimate resembles Lemma 3.1 of [27]. However, the different Carleman Weight Function we use here requires a different proof of the target estimate. In formulations and proofs of Carleman estimates below only for real valued functions u are used, since $|u|^2 = (\operatorname{Re} u)^2 + (\operatorname{Im} u)^2$ for complex valued ones.

Lemma 1. *For all real valued functions $u \in H^2(-b, b)$ such that $u(-b) = u'(-b) = 0$ and for all $\lambda \geq 1$ the following Carleman estimate holds:*

$$\begin{aligned} \int_{-b}^b (u'')^2 \mu_\lambda(z) dz &\geq C \int_{-b}^b (u'')^2 \mu_\lambda(z) dz \\ &\quad + C\lambda \int_{-b}^b (u')^2 \mu_\lambda(z) dz + C\lambda^3 \int_{-b}^b u^2 \mu_\lambda(z) dz. \end{aligned} \quad (28)$$

Here and below the constant $C > 0$ depends only on numbers r and b .

Proof. We prove this estimate for functions $u \in C^2[-b, b]$ satisfying $u(-b) = u'(-b) = 0$. Extension for the case $u \in H^2(-b, b)$ can be done using density arguments. Recall that $r > b$. Introduce the function $v = u \exp(\lambda(z - \theta)^2)$. Then $u = v \exp(-\lambda(z - \theta)^2)$. Hence,

$$u_{zz} = \left(v_{zz} - 4\lambda(z - \theta)v_z + 4\lambda^2(z - \theta)^2(1 + \mathcal{O}(1/\lambda))v \right) e^{-\lambda(z - \theta)^2}.$$

Here and below $\mathcal{O}(1/\lambda)$ denotes different C^2 -functions satisfying the estimate $|\mathcal{O}(1/\lambda)| \leq C/\lambda, \forall \lambda \geq 1$ together with their derivatives up to the second order. Therefore,

$$\begin{aligned} (u_{zz})^2 e^{2\lambda(z - \theta)^2} &= \left(v_{zz} - 4\lambda(z - \theta)v_z + 4\lambda^2(z - \theta)^2(1 + \mathcal{O}(1/\lambda))v \right)^2 \\ &\geq -8\lambda(z - \theta)v_z \left(v_{zz} + 4\lambda^2(z - \theta)^2(1 + \mathcal{O}(1/\lambda))v \right) \\ &= \left(-4\lambda(z - \theta)v_z^2 \right)_z + 4\lambda v_z^2 + \left(-16\lambda^3(z - \theta)^3(1 + \mathcal{O}(1/\lambda))v^2 \right)_z \\ &\quad + 48\lambda^3(z - \theta)^2(1 + \mathcal{O}(1/\lambda))v^2. \end{aligned} \quad (29)$$

Since $u(-b) = u'(-b) = 0$, then integrating the estimate (29) over $z \in (-b, b)$, we obtain

$$\int_{-b}^b (u_{zz})^2 e^{2\lambda(z - \theta)^2} dz \geq 4\lambda \int_{-b}^b v_z^2 dz + 47\lambda^3 \int_{-b}^b (z - \theta)^2 u^2 e^{2\lambda(z - \theta)^2} dz. \quad (30)$$

We have used here the fact that

$$\begin{aligned} \int_{-b}^b \left(-4\lambda(z - \theta)v_z^2 \right)_z dz &= -4\lambda(z - \theta) \left(u_z e^{\lambda(z - \theta)^2} + 2\lambda(z - \theta)u e^{\lambda(z - \theta)^2} \right)^2 \Big|_{z=-b}^{z=b} \\ &= -4\lambda(b - \theta) \left(u_z(b) + 2\lambda(b - \theta)u(b) \right)^2 e^{2\lambda(b - \theta)^2} \geq 0, \\ \int_{-b}^b \left(-16\lambda^3(z - \theta)^3(1 + \mathcal{O}(1/\lambda))v^2 \right)_z dz \\ &= -16\lambda^3(z - \theta)^3 u^2 e^{2\lambda(z - \theta)^2} (1 + \mathcal{O}(1/\lambda)) \Big|_{z=-b}^{z=b} \geq 15\lambda^3(r - \theta)^3 u^2(b) e^{2\lambda(b - \theta)^2} \geq 0. \end{aligned}$$

Now we take into account the first term on the right-hand side of (30). Using the Cauchy–Schwarz inequality, we estimate it from the below as:

$$4\lambda v_z^2 = 4\lambda \left[u_z e^{\lambda(z-\theta)^2} + 2\lambda(z-\theta) u e^{\lambda(z-\theta)^2} \right]^2 \geq 4\lambda \left(\frac{1}{2} u_z^2 e^{2\lambda(z-\theta)^2} - 4\lambda^2 (z-\theta)^2 u^2 e^{2\lambda(z-\theta)^2} \right).$$

Hence, using (30), we obtain

$$\int_{-b}^b (u_{zz})^2 e^{2\lambda(z-\theta)^2} dz \geq 2\lambda \int_{-b}^b u_z^2 e^{2\lambda(z-\theta)^2} dz + 31\lambda^3 (b-\theta)^2 \int_{-b}^b u^2 e^{2\lambda(z-\theta)^2} dz.$$

It easily follows from this estimate that

$$\int_{-b}^b (u_{zz})^2 e^{2\lambda(z-\theta)^2} dz \geq \frac{1}{2} \int_{-b}^b (u_{zz})^2 e^{2\lambda(z-\theta)^2} dz + \lambda \int_{-b}^b u_z^2 e^{2\lambda(z-\theta)^2} dz + 15\lambda^3 (b-\theta)^2 \int_{-b}^b u^2 e^{2\lambda(z-\theta)^2} dz.$$

Hence, we complete the proof of the lemma. \square

We now derive a Carleman estimate for the Laplace operator in partial finite differences. A similar Carleman estimate was proven in Theorem 7.1 of [30]. However, the CWF $\varphi_\lambda(z) = e^{-2\lambda z}$ in [30] is different from the one we use.

Theorem 1 (Carleman estimate in partial finite differences). *There exist a sufficient large constant $\lambda_0 = \lambda_0(\Omega, \theta) \geq 1$ and a number $C = C(\Omega, r, b) > 0$ depending only on listed parameters such that for all $\lambda \geq \lambda_0$ and for all vector functions $u^h \in H_{2N,0}^{2,h}(\Omega_h)$ the following Carleman estimate holds:*

$$\begin{aligned} & \sum_{p,q=1}^{Z_h-1} h^2 \int_{-b}^b \left(\Delta^h u_{p,q}^h(z) \right)^2 \mu_\lambda(z) dz \\ & \geq C \sum_{p,q=1}^{Z_h-1} h^2 \int_{-b}^b \left(\partial_z^2 u_{p,q}^h(z) \right)^2 \mu_\lambda(z) dz + C\lambda \sum_{p,q=1}^{Z_h-1} h^2 \int_{-b}^b \left(\partial_z u_{p,q}^h(z) \right)^2 \mu_\lambda(z) dz \\ & + C\lambda^3 \sum_{p,q=1}^{Z_h-1} h^2 \int_{-b}^b \left(\left(\nabla^h u_{p,q}^h(z) \right)^2 + \left(u_{p,q}^h(z) \right)^2 \right) \mu_\lambda(z) dz. \end{aligned} \quad (31)$$

Proof. Again, it is sufficient to prove (31) for $u(x_p, y_q, z) \in C^2[-b, b]$ for all (x_p, y_q) . Using the definitions of operators in partial finite differences (subsection 3.2.1) we obtain:

$$\begin{aligned} & \sum_{p,q=1}^{Z_h-1} h^2 \int_{-b}^b \left| \Delta^h u_{p,q}^h(z) \right|^2 \mu_\lambda(z) dz = \sum_{p,q=1}^{Z_h-1} h^2 \int_{-b}^b \left| \left(u_{zz}^h + u_{xx}^h + u_{yy}^h \right) (x_p, y_q, z) \right|^2 \mu_\lambda(z) dz \\ & \geq \frac{1}{2} \sum_{p,q=1}^{Z_h-1} h^2 \int_{-b}^b \left| \partial_z^2 u_{p,q}^h(z) \right|^2 \mu_\lambda(z) dz - h^2 \sum_{p,q=1}^{Z_h-1} \int_{-b}^b \left| \left(u_{xx}^h + u_{yy}^h \right) (x_p, y_q, z) \right|^2 \mu_\lambda(z) dz \\ & \geq \frac{1}{2} \sum_{p,q=1}^{Z_h-1} h^2 \int_{-b}^b \left| \partial_z^2 u_{p,q}^h(z) \right|^2 \mu_\lambda(z) dz - C \sum_{p,q=1}^{Z_h-1} \int_{-b}^b \left| u_{p,q}^h(z) \right|^2 \mu_\lambda(z) dz. \end{aligned}$$

Thus, the rest of the proof follows from Lemma 1. \square

3.2.3. Global strict convexity of the functional $J_{h,\lambda}(V^h)$ on the set $\overline{B(M)}$

Below, (\cdot, \cdot) is the scalar product in the space $H_{2N}^{2,h}(\Omega_h)$.

Theorem 2 (Global strict convexity: the central theorem of this paper). *Let $\lambda_0 > 1$ be the number of Theorem 1. For any $\lambda > 0$ the functional $J_{h,\lambda}(V^h)$ defined in (24) has its Frechét derivative $J'_{h,\lambda}(V^h) \in H_{2N,0}^{2,h}$ at any point $V^h \in \overline{B(M)}$. In addition, there exist numbers $\lambda_1 = \lambda_1(\Omega, \theta, N, M) \geq \lambda_0 > 1$ and $C_2 = C_2(\Omega_h, \theta, N, M) > 0$ depending only on listed parameters such that for all $\lambda \geq \lambda_1$ the functional $J_{h,\lambda}(V^h)$ is strictly convex on $\overline{B(M)}$. More precisely, the following estimate holds:*

$$J_{h,\lambda}(V^h + r^h) - J_{h,\lambda}(V^h) - J'_{h,\lambda}(V^h)(r^h) \geq C_2 e^{2\lambda(b-\theta)^2} \|r^h\|_{H_{2N}^{2,h}}^2 \quad \text{for all } V^h, V^h + r^h \in \overline{B(M)}. \quad (32)$$

Proof. Denote $\mathbf{x}^h = (x_p, y_q, z)$. For brevity, we do not indicate here the dependence of \mathbf{x}^h on indices p and q . Below $C_2 = C_2(\Omega_h, \theta, N, M) > 0$ denotes different positive constants depending only on listed parameters. Denote

$$B_0(M) = \left\{ W^h \in H_{2N,0}^{2,h} : \|W^h\|_{H_{2N}^{2,h}(\Omega_h)} < M \right\} \subset H_{2N,0}^{2,h}. \quad (33)$$

Let $V_{(1)}^h, V_{(2)}^h \in \overline{B(M)}$ be two arbitrary points. Denote $r^h = (r_1^h, r_2^h) = V_{(2)}^h - V_{(1)}^h$. Then

$$r^h \in \overline{B_0(2M)}. \quad (34)$$

Obviously, $\left| L(V_{(2)}^h) \right|^2 = \left| L(V_{(1)}^h + r^h) \right|^2$, where L is the operator defined in (19). Recall that by (18), the nonlinear term $K(\nabla V)$ in L is quadratic with respect to the components of ∇V . Hence,

$$\begin{aligned} L(V_{(1)}^h + r^h) &= \Delta^h V_{(1)}^h + \Delta^h r^h + K(\nabla^h V_{(1)}^h + \nabla^h r^h) \\ &= \Delta^h V_{(1)}^h + \Delta^h r^h + K(\nabla^h V_{(1)}^h) + K_1(\mathbf{x}^h) \nabla^h r^h + K_2(\mathbf{x}^h, \nabla^h r^h). \end{aligned}$$

Thus,

$$L(V_{(1)}^h + r^h) = L(V_{(1)}^h) + \Delta^h r^h + K_1(\mathbf{x}^h) \nabla^h r^h + K_2(\mathbf{x}^h, \nabla^h r^h). \quad (35)$$

Here, the vector functions K_1, K_2 are continuous with respect to \mathbf{x}^h in $\overline{\Omega}$. Moreover, $K_1(\mathbf{x}^h)$ is independent of r^h and $K_2(\mathbf{x}^h, \nabla^h r^h)$ is quadratic with respect to the components of $\nabla^h r^h$. It follows from (26) and the analog of (27) for $\overline{B_0(2M)}$ that

$$\left| K_2(\mathbf{x}^h, \nabla^h r^h) \right| \leq C_2 \left| \nabla^h r^h \right|^2 \quad \text{for all } \mathbf{x} \in \overline{\Omega}. \quad (36)$$

Obviously, for any pair $z_1, z_2 \in \mathbb{C}$ the following is true: $|z_1 + z_2|^2 = |z_1|^2 + |z_2|^2 + 2 \operatorname{Re}(\overline{z_1} z_2)$. Using this, we square the absolute value of both sides of (35) and obtain

$$\begin{aligned} \left| L^h(V_{(1)}^h + r^h) \right|^2 &= \left| L^h(V_{(1)}^h) \right|^2 + 2 \operatorname{Re} \left\{ \overline{L^h(V_{(1)}^h)} \left[\Delta^h r^h + K_1(\mathbf{x}^h) \nabla^h r^h + K_2(\mathbf{x}^h, \nabla^h r^h) \right] \right\} \\ &\quad + \left| \Delta^h r^h + K_1(\mathbf{x}^h) \nabla^h r^h + K_2(\mathbf{x}^h, \nabla^h r^h) \right|^2, \end{aligned}$$

which leads to

$$\begin{aligned}
& \left| L^h \left(V_{(1)}^h + r^h \right) \right|^2 - \left| L^h \left(V_{(1)}^h \right) \right|^2 \\
&= 2 \operatorname{Re} \left\{ \overline{L^h \left(V_{(1)}^h \right)} \left[\Delta^h r^h + K_1 \left(\mathbf{x}^h \right) \nabla^h r^h \right] \right\} + 2 \operatorname{Re} \left\{ \overline{L^h \left(V_{(1)}^h \right)} K_2 \left(\mathbf{x}^h, \nabla^h r^h \right) \right\} \\
&+ \left| \Delta^h r^h \right|^2 + 2 \operatorname{Re} \left\{ \overline{\Delta^h r^h} \left[K_1 \left(\mathbf{x}^h \right) \nabla^h r^h + K_2 \left(\mathbf{x}^h, \nabla^h r^h \right) \right] \right\} + \left| K_1 \left(\mathbf{x}^h \right) \nabla^h r^h + K_2 \left(\mathbf{x}^h, \nabla^h r^h \right) \right|^2.
\end{aligned} \tag{37}$$

The first term in the right hand side of equation (37) is linear with respect to r . Hence, using (24), we obtain

$$\begin{aligned}
& J_{h,\lambda} \left(V_{(1)}^h + r^h \right) - J_{h,\lambda} \left(V_{(1)}^h \right) = \operatorname{Lin} \left(r^h \right) \\
&+ \sum_{p,q=1}^{Z_h-1} h^2 \int_{-b}^b \left(\left| \Delta^h r^h \right|^2 + 2 \operatorname{Re} \left\{ \overline{\Delta^h r^h} \left[\left(K_1 \left(\mathbf{x}^h \right) \nabla^h r^h \right) + K_2 \left(\mathbf{x}^h, \nabla^h r^h \right) \right] \right\} \right) \mu_\lambda(z) dz \\
&+ \sum_{p,q=1}^{Z_h-1} h^2 \int_{-b}^b \left[2 \operatorname{Re} \left\{ \overline{L \left(V_{(1)}^h \right)} K_2 \left(\mathbf{x}^h, \nabla^h r^h \right) \right\} + \left| K_1 \left(\mathbf{x}^h \right) \nabla^h r^h + K_2 \left(\mathbf{x}^h, \nabla^h r^h \right) \right|^2 \right] \mu_\lambda(z) dz.
\end{aligned} \tag{38}$$

In (38), the linear functional $\operatorname{Lin} \left(r^h \right) : H_{2N,0}^{2,h} \rightarrow \mathbb{R}$ is given by

$$\operatorname{Lin} \left(r \right) = 2 \sum_{p,q=1}^{Z_h-1} h^2 \int_{-b}^b \operatorname{Re} \left\{ \overline{L \left(V_{(1)}^h \right)} \left[\Delta^h r + K_1 \left(\mathbf{x}^h \right) \nabla^h r \right] \right\} \mu_\lambda(z) dz.$$

We now estimate this functional from the above. Since $V_{(1)}^h \in \overline{B(M)}$ then the structure of K and (27) imply that $\left| K \left(\nabla V_{(1)}^h \right) \right| \leq C_2$. Hence, the Hölder inequality and (21) imply that

$$\begin{aligned}
|\operatorname{Lin} \left(r \right)| &\leq 2 \sum_{p,q=1}^{Z_h-1} h^2 \left(\int_{-b}^b \left| \Delta V_{(1)}^h + K \left(\nabla V_{(1)}^h \right) \right|^2 dz \right)^{1/2} \left(\int_{-b}^b \left| \Delta^h r^h + K_1 \left(\mathbf{x}^h \right) \nabla^h r^h \right|^2 dz \right)^{1/2} \\
&\leq 4C_2 e^{2\lambda(b+\theta)^2} \left\| r^h \right\|_{H_{2N}^{2,h}}.
\end{aligned}$$

Thus, the functional $\operatorname{Lin} \left(r^h \right) : H_{2N,0}^{2,h} \rightarrow \mathbb{R}$ is linear and bounded. Hence, by the Riesz theorem, there exists a unique point $\mathbf{P}^h \in H_{2N,0}^{2,h}$ independent of r^h such that

$$\operatorname{Lin} \left(r^h \right) = \left(\mathbf{P}^h, r^h \right) \quad \text{for all } r^h \in H_{2N,0}^{2,h}.$$

Next, using the Cauchy–Schwarz inequality and (36), we find that

$$2 \operatorname{Re} \left\{ \overline{\Delta^h r^h} \left[\left(K_1 \left(\mathbf{x}^h \right) \nabla^h r^h \right) + K_2 \left(\mathbf{x}^h, \nabla^h r^h \right) \right] \right\} \leq \frac{1}{2} \left| \Delta^h r^h \right|^2 + C_2 \left| \nabla^h r^h \right|^2. \tag{39}$$

In addition, we have

$$\left| 2 \operatorname{Re} \left\{ \overline{L^h \left(V_{(1)}^h \right)} K_2 \left(\mathbf{x}^h, \nabla^h r^h \right) \right\} \right| + \left| K_1 \left(\mathbf{x}^h \right) \nabla^h r^h + K_2 \left(\mathbf{x}^h, \nabla^h r^h \right) \right|^2 \leq C_2 \left| \nabla^h r^h \right|^2. \tag{40}$$

Combining (38), (39) and (40), we easily obtain

$$\left| J_{h,\lambda} \left(V_{(1)}^h + r \right) - J_{h,\lambda} \left(V_{(1)}^h \right) - \left(\mathbf{P}^h, r \right) \right| \leq C_2 \left\| r^h \right\|_{H_{2N}^{2,h}}^2.$$

Henceforth, $\mathbf{P}^h \in H_{2N,0}^{2,h}$ is actually the Frechét derivative of the cost functional $J_{h,\lambda}$ at the point $V_{(1)}^h \in \overline{B(M)}$, i.e. $\mathbf{P}^h = J'_{h,\lambda} \left(V_{(1)}^h \right) \in H_{2N,0}^{2,h}$.

We now focus on the proof of the target estimate (32). To do so, we estimate from below the second and third terms on the right hand side of (38). In fact, using (39) we get

$$\begin{aligned} & \sum_{p,q=1}^{Z_h-1} h^2 \int_{-b}^b \left(\left| \Delta^h r^h \right|^2 + 2 \operatorname{Re} \left\{ \overline{\Delta^h r^h} \left[\left(K_1 \left(\mathbf{x}^h \right) \nabla^h r^h \right) + K_2 \left(\mathbf{x}^h, \nabla^h r^h \right) \right] \right\} \right) \mu_\lambda(z) dz \\ & \geq \frac{1}{2} \sum_{p,q=1}^{Z_h-1} h^2 \int_{-b}^b \left| \Delta^h r^h \right|^2 \mu_\lambda(z) dz - C_2 \sum_{p,q=1}^{Z_h-1} h^2 \int_{-b}^b \left| \nabla^h r^h \right|^2 \mu_\lambda(z) dz. \end{aligned} \quad (41)$$

Similarly, using (36), we estimate the third term in the right hand side of (38) as

$$\begin{aligned} & \sum_{p,q=1}^{Z_h-1} h^2 \int_{-b}^b \left[2 \operatorname{Re} \left\{ \overline{L^h \left(V_{(1)}^h \right)} K_2 \left(\mathbf{x}^h, \nabla^h r^h \right) \right\} + \left| K_1 \left(\mathbf{x}^h \right) \nabla^h r^h + K_2 \left(\mathbf{x}^h, \nabla^h r^h \right) \right|^2 \right] \mu_\lambda(z) dz \\ & \geq -C_2 \sum_{p,q=1}^{Z_h-1} h^2 \int_{-b}^b \left| \nabla^h r^h \right|^2 \mu_\lambda(z) dz. \end{aligned} \quad (42)$$

Thus, combining (38) and (42), we obtain

$$\begin{aligned} & J_{h,\lambda} \left(V_{(1)}^h + r^h \right) - J_{h,\lambda} \left(V_{(1)}^h \right) - \left(J'_{h,\lambda} \left(V_{(1)}^h \right), r^h \right) \\ & \geq \left[\frac{1}{2} \sum_{p,q=1}^{Z_h-1} h^2 \int_{-b}^b \left| \Delta^h r_{p,q}^h \right|^2 \mu_\lambda(z) dz - C_2 \sum_{p,q=1}^{Z_h-1} h^2 \int_{-b}^b \left| \nabla^h r_{p,q}^h \right|^2 \mu_\lambda(z) dz \right]. \end{aligned} \quad (43)$$

Since the function $r \in H_{2N,0}^{2,h}$, we now can apply to (43) the Carleman estimate (31). Prior to that, we note that we can find a sufficiently large number $\tilde{\lambda}_0 = \tilde{\lambda}_0(\Omega, \theta, N, M) \geq \lambda_0 > 1$ such that for all $\lambda \geq \tilde{\lambda}_0$

$$\begin{aligned} & \frac{1}{2} \sum_{p,q=1}^{Z_h-1} h^2 \int_{-b}^b \left| \Delta^h r_{p,q}^h \right|^2 \mu_\lambda(z) dz - C_2 \sum_{p,q=1}^{Z_h-1} h^2 \int_{-b}^b \left| \nabla^h r_{p,q}^h \right|^2 \mu_\lambda(z) dz \\ & \geq C \sum_{p,q=1}^{Z_h-1} h^2 \int_{-b}^b \left| \partial_z^2 r_{p,q}^h(z) \right|^2 \mu_\lambda(z) dz + C\lambda \sum_{p,q=1}^{Z_h-1} h^2 \int_{-b}^b \left| \partial_z r_{p,q}^h(z) \right|^2 \mu_\lambda(z) dz \\ & + C\lambda^3 \sum_{p,q=1}^{Z_h-1} h^2 \int_{-b}^b \left(\left| \nabla^h r_{p,q}^h(z) \right|^2 + \left| r_{p,q}^h(z) \right|^2 \right) \mu_\lambda(z) dz - C_2 \sum_{p,q=1}^{Z_h-1} h^2 \int_{-b}^b \left| \nabla^h r_{p,q}^h \right|^2 \mu_\lambda(z) dz. \end{aligned}$$

Hence, choosing $\lambda_1 = \lambda_1(\Omega_h, \theta, N, M) \geq \tilde{\lambda}_0 > 1$ such that $C\lambda_1 > 2C_2$, we obtain

$$\begin{aligned} & \frac{1}{2} \sum_{p,q=1}^{Z_h-1} h^2 \int_{-b}^b \left| \Delta^h r_{p,q}^h \right|^2 \mu_{\lambda_1}(z) dz - C_2 \sum_{p,q=1}^{Z_h-1} h^2 \int_{-b}^b \left| \nabla^h r_{p,q}^h \right|^2 \mu_{\lambda_1}(z) dz \\ & \geq C_2 \sum_{p,q=1}^{Z_h-1} h^2 \int_{-b}^b \left| \partial_z^2 r_{p,q}^h(z) \right|^2 \mu_{\lambda_1}(z) dz + C_2\lambda \sum_{p,q=1}^{Z_h-1} h^2 \int_{-b}^b \left(\left| \partial_z r_{p,q}^h(z) \right|^2 + \left| r^h(z) \right|^2 \right) \mu_{\lambda_1}(z) dz. \end{aligned} \quad (44)$$

Thus, it follows from (43), (44) and (22) that for all $\lambda \geq \lambda_1$

$$J_{h,\lambda}(V_{(1)}^h + r^h) - J_{h,\lambda}(V_{(1)}^h) - (J'_{h,\lambda}(V_{(1)}^h), r^h) \geq C_2 e^{2\lambda(b-\theta)^2} \|r^h\|_{H_{2N}^{2,h}}^2. \quad (45)$$

Estimate (45) completes the proof of this theorem. \square

We now formulate a theorem about the Lipschitz continuity of the Frechét derivative $J'_{h,\lambda}(V^h)$ on $\overline{B(M)}$. We omit the proof of this result because it is similar to the proof of Theorem 3.1 in [3].

Theorem 3. *The Frechét derivative $J'_{h,\lambda}(V^h)$ constructed in the proof of Theorem 2 satisfies the Lipschitz continuity condition on the set $\overline{B(M)}$. More precisely, there exists a number $\widehat{C} = \widehat{C}(\Omega, \theta, N, M, \lambda) > 0$ depending only on listed parameters such that for any pair $V_{(1)}^h, V_{(2)}^h \in \overline{B(M)}$ the following estimate holds:*

$$\|J'_{h,\lambda}(V_{(2)}^h) - J'_{h,\lambda}(V_{(1)}^h)\|_{H_{2N}^{2,h}} \leq \tilde{C} \|V_{(2)}^h - V_{(1)}^h\|_{H_{2N}^{2,h}}.$$

As to the existence and uniqueness of the minimizer, they are established in the following theorem. This theorem follows from a combination of Theorems 2 and 3 with Lemma 2.1 and Theorem 2.1 of [3]. Therefore, we omit its proof.

Theorem 4. *Let $\lambda_1 > 1$ be the number chosen in Theorem 2. Then there exists a unique minimizer $V_{\min,\lambda}^h \in \overline{B(M)}$ of the functional $J'_{h,\lambda}(V^h)$ on the set $\overline{B(M)}$. Furthermore, the following inequality holds:*

$$(J'_{h,\lambda}(V_{\min,\lambda}^h), V_{\min,\lambda}^h - Q) \leq 0 \quad \text{for all } Q \in \overline{B(M)}. \quad (46)$$

3.3. Convergence rate of regularized solutions

Using (25), we obtain the following analog of problem (14)–(16) in partial finite differences is:

$$L^h(V^h(z)) = \Delta^h V^h(\mathbf{x}^h) + K(\nabla^h V^h(\mathbf{x}^h)) = 0 \quad \text{for } \mathbf{x}^h \in \Omega_h, \quad (47)$$

$$\nabla^h V^h(\mathbf{x}^h) \cdot \mathbf{n} = 0 \quad \text{for } \mathbf{x}^h \in \partial\Omega_h \setminus \Gamma_h, \quad (48)$$

$$V(\mathbf{x}^h) = \psi_0^h(\mathbf{x}^h), V_z(\mathbf{x}^h) = \psi_1(\mathbf{x}^h) \quad \text{for } \mathbf{x}^h \in \Gamma_h. \quad (49)$$

Following the Tikhonov regularization concept (cf. e.g. [45]), we assume that there exists an exact solution $V_*^h \in H_{2N}^{2,h}$ of problem (47)–(49) with the noiseless data $\psi_{0*}^h(\mathbf{x}^h)$ and $\psi_{1*}^h(\mathbf{x}^h)$. To this end, the subscript “*” is only used for the exact solution. In applications the data $\psi_0^h(\mathbf{x}^h)$ and $\psi_1^h(\mathbf{x}^h)$ are noise-contaminated.

We, therefore, denote by $\delta \in (0, 1)$ the level of noise in those data. We assume that

$$\|V_*^h\|_{H_{2N}^{2,h}} < M - \delta. \quad (50)$$

In accordance with the regularization theory (cf. e.g. [45]), given the value of δ , the minimizer $V_{\min,\lambda}^h$ of the functional $J_{h,\lambda}(V^h)$, which was found in Theorem 4, is called the *regularized solution* of problem (47)–(49). We want to estimate the δ –dependence of the norm $\|V_*^h - V_{\min,\lambda}^h\|_{H_{2N}^{2,h}}$, i.e. we want to estimate

the convergence rate of regularized solutions, which also means the accuracy estimate of the minimizer $V_{\min,\lambda}^h$. To do this, we assume that there exist two vector functions $\Psi_*^h, \Psi^h \in H_{2N}^{2,h}$ such that

$$\nabla^h \Psi_*^h(\mathbf{x}^h) \cdot \mathbf{n} = 0, \quad \nabla^h \Psi^h(\mathbf{x}^h) \cdot \mathbf{n} = 0 \quad \text{for } \mathbf{x}^h \in \partial\Omega_h \setminus \Gamma_h, \quad (51)$$

$$\Psi_*^h(\mathbf{x}^h) = \psi_{0*}^h(\mathbf{x}^h), \quad \Psi_{z*}^h(\mathbf{x}^h) = \psi_{1*}^h(\mathbf{x}^h) \quad \text{for } \mathbf{x}^h \in \Gamma_h, \quad (52)$$

$$\Psi^h(\mathbf{x}^h) = \psi_0^h(\mathbf{x}^h), \quad \Psi_z^h(\mathbf{x}^h) = \psi_1^h(\mathbf{x}^h) \quad \text{for } \mathbf{x}^h \in \Gamma_h, \quad (53)$$

$$\left\| \Psi_*^h \right\|_{H_{2N}^{2,h}} < M, \quad \left\| \Psi^h \right\|_{H_{2N}^{2,h}} < M, \quad (54)$$

$$\left\| \Psi^h - \Psi_*^h \right\|_{H_{2N}^{2,h}} < \delta. \quad (55)$$

Theorem 5 (convergence rate of regularized solutions). *Assume that conditions (50)–(55) are valid. Let $\lambda_1 = \lambda_1(\Omega, \theta, N, M) > 1$ be the number of Theorem 3. Let $V_{\min,\lambda}^h \in \overline{B(M)}$ be the minimizer of functional (24) which is found in Theorem 4. Then the following accuracy estimate holds for all $\lambda \geq \lambda_1$*

$$\left\| V_{\min,\lambda}^h - V_*^h \right\|_{H_{2N}^{2,h}} \leq C_2 \delta e^{4\lambda b \theta}. \quad (56)$$

Proof. Denote

$$W_{\min,\lambda}^h = V_{\min,\lambda}^h - \Psi^h, \quad W_*^h = V_*^h - \Psi_*^h. \quad (57)$$

Hence, by (33) and (54)

$$W_{\min,\lambda}^h, W_*^h \in B_0(2M). \quad (58)$$

It follows from (50)–(57) and the triangle inequality that

$$\begin{aligned} \left\| W_*^h + \Psi^h \right\|_{H_{2N}^{2,h}} &= \left\| W_*^h + \Psi_*^h + (\Psi^h - \Psi_*^h) \right\|_{H_{2N}^{2,h}} \leq \left\| W_*^h + \Psi_*^h \right\|_{H_{2N}^{2,h}} + \delta \\ &< M - \delta + \delta = M. \end{aligned}$$

Denote

$$\tilde{V}_*^h = W_*^h + \Psi^h. \quad (59)$$

Hence, (26), (52), (53), (58) and (59) imply that

$$W_*^h + \Psi^h = \tilde{V}_*^h \in B(M). \quad (60)$$

By (47), it holds that $L^h(V_*^h) = 0$. Hence, $L^h(W_*^h + \Psi^h) = L^h(V_*^h) = 0$. Hence, by (24) we have

$$J_{h,\lambda}(V_*^h) = 0. \quad (61)$$

Next, by (32) and (60) we estimate that

$$J_{h,\lambda}(\tilde{V}_*^h) - J_{h,\lambda}(V_{\min,\lambda}^h) - J'_{h,\lambda}(V_{\min,\lambda}^h)(\tilde{V}_*^h - V_{\min,\lambda}^h) \geq C_2 e^{2\lambda(b-\theta)^2} \left\| \tilde{V}_*^h - V_{\min,\lambda}^h \right\|_{H_{2N}^{2,h}}^2. \quad (62)$$

It follows from (46) that $-J'_{h,\lambda}(V_{\min,\lambda}^h)(\tilde{V}_*^h - V_{\min,\lambda}^h) \leq 0$. This implies that

$$J_{h,\lambda}(\tilde{V}_*^h) - J_{h,\lambda}(V_{\min,\lambda}^h) - J'_{h,\lambda}(V_{\min,\lambda}^h)(\tilde{V}_*^h - V_{\min,\lambda}^h) \leq J_{h,\lambda}(\tilde{V}_*^h).$$

The latter and (62) lead to

$$\left\| \tilde{V}_*^h - V_{\min, \lambda}^h \right\|_{H_{2N}^{2,h}}^2 \leq C_2 e^{-2\lambda(b-\theta)^2} J_{h, \lambda} \left(\tilde{V}_*^h \right). \quad (63)$$

We now estimate $J_{h, \lambda} \left(\tilde{V}_*^h \right)$ from the above. By (24), (47), (55), (61) and (59) it yields

$$\begin{aligned} J_{h, \lambda} \left(\tilde{V}_*^h \right) &= \sum_{p, q=1}^{Z_h-1} h^2 \int_{-b}^b \left| L^h \left(\tilde{V}_*^h(z) \right) \right|^2 \mu_\lambda(z) dz \\ &= \sum_{p, q=1}^{Z_h-1} h^2 \int_{-b}^b \left| L^h \left(W_*^h(z) + \Psi_*^h(z) \right) + \left(\Psi^h(z) - \Psi_*^h(z) \right) \right|^2 \mu_\lambda(z) dz \\ &= \sum_{p, q=1}^{Z_h-1} h^2 \int_{-b}^b \left| L^h \left(V_*^h(z) \right) \right|^2 \mu_\lambda(z) dz + \sum_{p, q=1}^{Z_h-1} h^2 \int_{-b}^b S^h(z) \mu_\lambda(z) dz \\ &= \sum_{p, q=1}^{Z_h-1} h^2 \int_{-b}^b S^h(z) \mu_\lambda(z) dz. \end{aligned}$$

In view of the fact that

$$\sum_{p, q=1}^{Z_h-1} h^2 \int_{-b}^b \left| S^h(z) \right| \mu_\lambda(z) dz \leq C_2 \delta^2 \max_{[-b, b]} \mu_\lambda(z),$$

we then use (21) to obtain

$$J_{h, \lambda} \left(\tilde{V}_*^h \right) \leq \sum_{p, q=1}^{Z_h-1} h^2 \int_{-b}^b \left| S^h(z) \right| \mu_\lambda(z) dz \leq C_2 \delta^2 \exp \left(2\lambda(b+\theta)^2 \right). \quad (64)$$

Combining estimates (63) and (64), we obtain the target estimate (56) of this theorem. \square

3.4. Global convergence of the gradient projection method

Just as in the previous section, we still assume the existence of vector functions V_*^h, Ψ_*^h and Ψ^h satisfying conditions formulated in that section. Similarly with (57), for each $V^h \in B(M)$ consider the vector function $W^h = V^h - \Psi^h$. Then (54) and the triangle inequality imply that, similarly with (58),

$$W^h \in B_0(2M) \subset H_{2N, 0}^{2,h} \quad \text{for all } V^h \in B(M), \quad (65)$$

$$W^h + \Psi^h \in B(3M) \quad \text{for all } W^h \in B_0(2M). \quad (66)$$

Consider the functional $I_{h, \lambda} : B_0(2M) \rightarrow \mathbb{R}$ defined as

$$I_{h, \lambda} \left(W^h \right) = J_{h, \lambda} \left(W^h + \Psi^h \right) \quad \text{for all } W^h \in B_0(2M). \quad (67)$$

We omit the proof of Theorem 6 since it follows immediately from Theorems 3–5 and (65)–(67).

Theorem 6. *For any $\lambda > 0$ the functional $I_{h, \lambda} \left(W^h \right)$ has its Frechét derivative $I'_{h, \lambda} \left(W^h \right) \in H_{2N, 0}^{2,h}$ at any point $W^h \in \overline{B_0(2M)}$ and this derivative is Lipschitz continuous on $\overline{B_0(2M)}$. Let $\lambda_1 = \lambda_1(\Omega, \theta, N, M) > 1$ and $C_2 = C_2(\Omega_h, \theta, N, M) > 0$ be the numbers of Theorem 3. Denote $\lambda = \lambda_1(\Omega, \theta, N, 3M) > 1$ and*

$\tilde{C}_2 = C_2(\Omega_h, \theta, N, 3M) > 0$. Then for any $\lambda \geq \tilde{\lambda}$ the functional $I_{h,\lambda}(W^h)$ is strictly convex on the ball $B_0(2M) \subset H_{2N,0}^{2,h}$, i.e. the following analog of estimate (32) is valid for all $W^h, W^h + r^h \in \overline{B_0(2M)}$:

$$I_{h,\lambda}(W^h + r^h) - I_{h,\lambda}(W^h) - I'_{h,\lambda}(W^h)(r^h) \geq \tilde{C}_2 e^{2\lambda(b-\theta)^2} \|r^h\|_{H_{2N}^{2,h}}^2.$$

Furthermore, there exists a unique minimizer $W_{\min,\lambda}^h$ of the functional $I_{h,\lambda}(W^h)$ on the set $\overline{B_0(2M)}$ and the following inequality holds:

$$\left(I'_{h,\lambda}(W_{\min,\lambda}^h), W_{\min,\lambda}^h - Q \right) \leq 0 \quad \text{for all } Q \in \overline{B_0(2M)}.$$

On top of that, let $Y_{\min,\lambda}^h = W_{\min,\lambda}^h + \Psi^h$. Then the direct analog of (56) holds where $V_{\min,\lambda}^h$ is replaced with $Y_{\min,\lambda}^h$.

We now construct the gradient projection method of the minimization of the functional $I_{h,\lambda}(W^h)$ on the set $\overline{B_0(2M)}$. Let $P : H_{2N,0}^{2,h} \rightarrow \overline{B_0(2M)}$ be the orthogonal projection operator. Let $W_0^h \in B_0(2M)$ be an arbitrary point of this ball. Let $\gamma \in (0, 1)$ be a number, which we will choose in Theorem 7. The sequence of the gradient projection method is:

$$W_{n,\lambda,\gamma}^h = \mathbf{P} \left(W_{n-1,\lambda,\gamma}^h - \gamma I'_{h,\lambda}(W_{n-1,\lambda,\gamma}^h) \right), \quad n = 1, 2, \dots \quad (68)$$

Note that since by Theorem 6, we have $I'_{h,\lambda}(W_{n-1,\lambda,\gamma}^h) \in H_{2N,0}^{2,h}$ and also since $W_{n-1,\lambda,\gamma}^h \in \overline{B_0(2M)} \subset H_{2N,0}^{2,h}$, then all three terms in (68) belong to $H_{2N,0}^{2,h}$, i.e. zero boundary conditions (48), (49) are satisfied for these functions.

Theorem 7 (the global convergence of the gradient projection method). *Assume that conditions of Theorem 6 hold and let $\lambda \geq \tilde{\lambda}$. Then there exists a number $\gamma_0 = \gamma_0(\Omega_h, \theta, N, 3M) \in (0, 1)$ depending only on listed parameters such that for every $\gamma \in (0, \gamma_0)$ there exists a number $\xi = \xi(\gamma) \in (0, \gamma_0)$ depending on γ such that for these values of γ the sequence (68) converges to $W_{\min,\lambda}^h$ and the following convergence rate holds:*

$$\|W_{n,\lambda,\gamma}^h - W_{\min,\lambda}^h\|_{H_{2N}^{2,h}} \leq \xi^n \|W_{\min,\lambda}^h - W_0^h\|_{H_{2N}^{2,h}}. \quad (69)$$

In addition,

$$\|W_*^h - W_{n,\lambda,\gamma}^h\|_{H_{2N}^{2,h}} \leq \tilde{C}_2 \delta e^{4\lambda b \theta} + \xi^n \|W_{\min,\lambda}^h - W_0^h\|_{H_{2N}^{2,h}}. \quad (70)$$

Now, let $c^h(\mathbf{x}^h)$ be the function $c(\mathbf{x})$ obtained after the substitution of components of the vector function V^h in equation (10) for a certain position of the point source \mathbf{x}_α (Remark 3). More precisely, let $c_{n,\lambda,\gamma}^h(\mathbf{x}^h)$ be obtained after the substitution of the components of the vector function $V_{n,\lambda,\gamma}^h = W_{n,\lambda,\gamma}^h + \Psi^h$ and let $c_*^h(\mathbf{x}^h)$ be obtained after the substitution of the components of the vector function $V_*^h = W_*^h + \Psi_*^h$. Then the following convergence estimate is valid

$$\|c_*^h - c_{n,\lambda,\gamma}^h\|_{L_{2N}^{2,h}} \leq \tilde{C}_2 \delta e^{4\lambda b \theta} + \xi^n \|W_{\min,\lambda}^h - W_0^h\|_{H_{2N}^{2,h}}. \quad (71)$$

Proof. Estimate (69) follows immediately from a combination of Theorem 6 with Theorem 2.1 of [3]. Estimate (70) is immediately implied by (69) and an obvious modification of the proof of estimate (56). More precisely, in this modification the minimizer $V_{\min,\lambda}^h$ of functional (24) should be replaced with $Y_{\min,\lambda}^h = W_{\min,\lambda}^h + \Psi^h$: recall that $W_{\min,\lambda}^h$ is the minimizer of the functional $I_{h,\lambda}(W^h)$ on the set $\overline{B_0(2M)}$. Finally, (71) follows from (10) and (70). \square

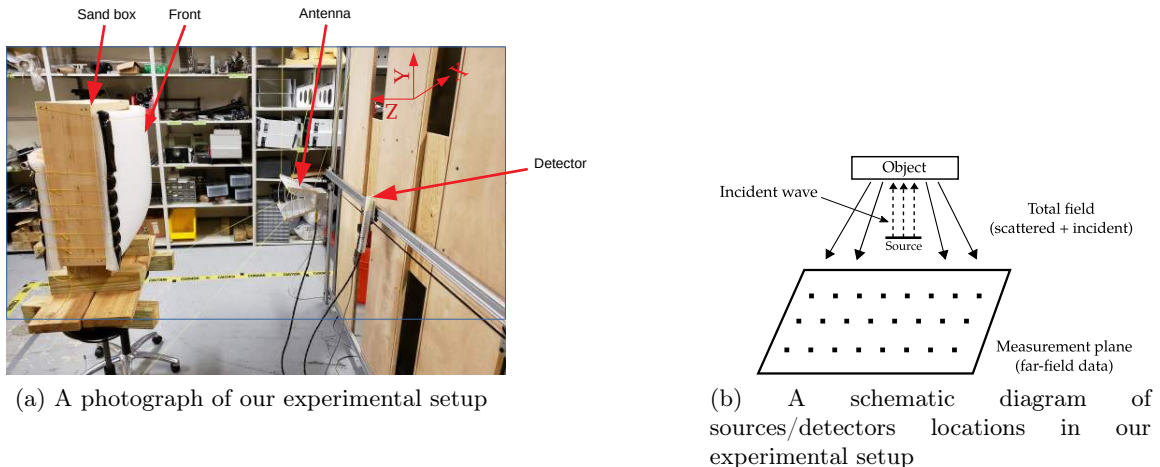


Figure 1: Our experimental setup (left) and a schematic diagram of our measurements (right).

Remark 5. Since the radius of the ball $\overline{B_0(2M)}$ is $2M$, where M is an arbitrary number and since the starting point W_0^h of iterations of the sequence (68) is an arbitrary point of $B_0(2M)$, then Theorem 7 actually claims the *global convergence* of the sequence (68) to the exact solution, as long as the level δ of the noise in the data tends to zero; see the second paragraph of the Introduction for the definition of the global convergence.

4. Experimental Results

4.1. Experimental setup

We now explain our experimental setup and data acquisition at the microwave facility of University of North Carolina at Charlotte (UNCC). Keeping in mind our target application mentioned in the first paragraph of Introduction to imaging of explosive-like devices, We have collected experimental data for objects buried in a sandbox. More precisely, we have placed the targets of interest inside of a wooden framed box filled with the moisture free sand. Besides, we cover the front and back sides of the sandbox by Styrofoam whose dielectric constant is close to 1, i.e. to the dielectric constant of air. Hence, Styrofoam should not affect neither the incident nor the scattered electric waves. Here, the front surface is physically defined as the foam layer closer to the transmitter fixed at a given position. On the other hand, the burial depths of objects do not exceed 10 cm, which really mimics a scanning and detecting action for shallow mine-like targets. Typically the sizes of antipersonnel land mines and improvised explosive devices are between 5 and do 15 centimeters (cm), see, e.g. [37]. The transmitter is a standard horn antenna, whose length is about 20 cm, and the detector is essentially a point probe. To get a better insight into the description we have detailed, the reader can take a look at Figure 1.

It is worth mentioning that there are several challenges that we confront in this configuration, which actually reflect the difficulties met in the realistic detection of land mines. We now name some central challenges:

- **Distractions.** Cf. Figure 1a, we deliberately keep many other devices and items (made of different materials) on the desks outside the yellow caution bands. In other words, we do not use any isolations of our device from the outside World. This is reasonable since no isolation conditions can be created on a battlefield. Obviously, such unwanted obstacles and furniture can affect the quality of the raw backscatter. The presence of the Wi-Fi signal is also unavoidable in the room where we conduct the

experiments. Moreover, it is technically very hard to place the antenna behind the measurement site. Therefore, the backscatter wave hits the antenna first and only then comes to detectors, which is another complicating factor.

- **Random noise factor.** When facing real experiments, one cannot rarely estimate the noise level as well as its frequency dependent dynamics since they depends on hundreds of factors such as measurement process, unknown true data, distracting signals, etc.

4.2. Buried targets to be imaged

We present here five (5) examples of computational reconstructions of buried objects mimicking typical metallic and non-metallic land mines. The tested objects we use in the experiments are basic in-store items that one can easily purchase. The burial depth of any target is not of an interest here since all depths are just a few centimeters. The most valuable information for the engineering part is in estimating the values of dielectric constants of targets as well as their shapes.

Our five examples are:

- Example 1: An aluminum cylinder (see Figure 2c). As metallic mines usually caught in military services, this object can be shaped as the NO-MZ 2B, a Vietnamese anti-personnel fragmentation mine; cf. e.g. [5]. It is known that metallic objects can be characterized by large values of dielectric constants [35]. Hence, we suppose that the true values of dielectric constants of metallic objects are large and are not fixed.
- Example 2: A glass bottle filled with the clear water (see Figure 3c). This object is more complicated than the one of Example 2 due to the presence of the cap on the top of the bottle. Example 2 is a good fit of the usual Glassmine 43 (cf. [42]), a non-metallic anti-personnel land mine largely with a glass body that the Germans used to make detection harder in the World War II era. The true value of the dielectric constant in this case was measured to be 23.8 [44].
- Example 3: An U-shaped piece of a dry wood (see Figure 4c). This example is our next attempt to deal with a non-metallic object. Note that the shape is non convex now. In the spirit of Example 2, this wood-based object is well-suited (in terms of the material) to the case of Schu-mine 42, an anti-personnel blast mine that the Germans developed during the World War II. The augmented complexity of the geometry of the object is just our purpose of this work since we wish to see how the reconstruction works with different front shapes. In this circumstance, the maximal achievable value of the dielectric constant which we see in [43] should be 6.
- Examples 4 and 5: Metallic letters “A” and “O” (see Figures 5c and 6c). Shapes are non convex. These two tests are different from the above examples because they were **blind** tests. This means that we did not know any other information except of the measured data and the fact that these objects were buried close to the sand surface. Since they are metallic, the true contrast should be large as in Example 1.

4.3. The necessity of data propagation

In the experimental setup, our observed and measured data are the source dependent backscattering data of the electric field. Although our experimental device measures the backscattering data with varied frequencies for each location of the point source, we use only a single frequency for each experiment when solving our CIP. Basically, these are varied far-field data; see Figures 1. However, these data are deficient, i.e. it is unlikely that these data can be reasonably inverted; see Figures 2a–6a. In fact, the same observation was made in previous publications of our research group on experimental data [30, 37, 44].

Hence, to make our data feasible for inversion, we apply the well known data propagation procedure which approximates the near field data. These approximate data form actual inputs of our minimization process. A rigorous justification of the data propagation procedure can be found in [37].

It is our experience that the good quality near-field data are not always obtained well enough from any far field data after the propagation. This requires a substantial workload in choosing proper data among a large amount of frequency dependent data sets. In other words, we have no choice but to select an acceptable frequency for each particular target we work with. So, we select its own frequency for each considered target. Then we use this frequency for all positions of the source we work with; see section 4.5 about particular choices of frequencies. A particular choice of an admissible and acceptable set of data has been illustrated in [37], and below this strategy will be confirmed again.

4.4. Data propagation revisited

We know in advance that the half space $\{z < -b\} \subset \mathbb{R}^3$ is homogeneous, i.e. $c(\mathbf{x}) = 1$ in this half space. Therefore, the function u_s is a backscatter wave in $\{z < -b\}$ and it satisfies the following conditions:

$$\begin{cases} \Delta u_s + k^2 u_s = 0 & \text{for } \mathbf{x} \in \{z < -b\}, \\ \partial_r u_s - i k u_s = \mathcal{O}(r^{-1}) & \text{for } r = |\mathbf{x} - \mathbf{x}_\alpha|, i = \sqrt{-1}. \end{cases} \quad (72)$$

As was mentioned in section 3.1, we actually measure the far field data, i.e. the function $u_s(x, y, -D, \mathbf{x}_\alpha)$, where the number $D > b$. Having the function $u_s(x, y, -D, \mathbf{x}_\alpha)$, we want approximate the function $u_s(x, y, -b, \mathbf{x}_\alpha)$, i.e. we want to approximate the wave field in the near field zone. The data propagation procedure does exactly this. Denote

$$u_s(x, y, -b, \mathbf{x}_\alpha) = \mathbf{U}(x, y, \mathbf{x}_\alpha) \text{ and } u_s(x, y, -D, \mathbf{x}_\alpha) = \mathbf{V}(x, y, \mathbf{x}_\alpha). \quad (73)$$

In this work, we rely on the data propagation procedure to unveil this difficulty as it has been successfully exploited in [37]. First, we apply the Fourier transform of the scattered field with respect to x, y , assuming that the corresponding integral converges:

$$\hat{u}_s(\rho_1, \rho_2, z, \mathbf{x}_\alpha) = \frac{1}{2\pi} \int_{\mathbb{R}^2} u_s(x, y, z, \mathbf{x}_\alpha) e^{-i(x\rho_1 + y\rho_2)} dx dy \quad \text{for } \rho_1, \rho_2 \in \mathbb{R}. \quad (74)$$

Next, we apply this Fourier transform to the PDE in (72) and arrive at a second order ODE with respect to z :

$$\partial_{zz}^2 \hat{u}_s + (k^2 - \rho_1^2 - \rho_2^2) \hat{u}_s = 0 \quad \text{for } z < -b. \quad (75)$$

By (73), we also have

$$\hat{u}_s(\rho_1, \rho_2, -b, \mathbf{x}_\alpha) = \hat{\mathbf{U}}(\rho_1, \rho_2, \mathbf{x}_\alpha) \text{ and } \hat{u}_s(\rho_1, \rho_2, -D, \mathbf{x}_\alpha) = \hat{\mathbf{V}}(\rho_1, \rho_2, \mathbf{x}_\alpha).$$

It follows from (75) that

$$\hat{u}_s(\rho_1, \rho_2, z, \mathbf{x}_\alpha) = \begin{cases} \hat{\mathbf{U}}(\rho_1, \rho_2, \mathbf{x}_\alpha) e^{\sqrt{\rho_1^2 + \rho_2^2 - k^2}(z+b)} & \text{if } \rho_1^2 + \rho_2^2 > k^2, \\ C_1 e^{-i\sqrt{k^2 - \rho_1^2 - \rho_2^2}(z+b)} + C_2 e^{i\sqrt{k^2 - \rho_1^2 - \rho_2^2}(z+b)} & \text{if } \rho_1^2 + \rho_2^2 < k^2, \end{cases}$$

where $z < -b$. It is not immediately clear which of two terms in the second line of the last formula should be taken. However, it was proven in Theorem 4.1 of [37] that only the first term which should be taken and one should set $C_2 := 0$. Thus, for $z < -b$

$$\hat{u}_s(\rho_1, \rho_2, z, \mathbf{x}_\alpha) = \begin{cases} \hat{\mathbf{U}}(\rho_1, \rho_2, \mathbf{x}_\alpha) e^{\sqrt{\rho_1^2 + \rho_2^2 - k^2}(z+b)} & \text{if } \rho_1^2 + \rho_2^2 > k^2, \\ \hat{\mathbf{U}}(\rho_1, \rho_2, \mathbf{x}_\alpha) e^{-i\sqrt{k^2 - \rho_1^2 - \rho_2^2}(z+b)} & \text{otherwise.} \end{cases} \quad (76)$$

Observe that if the Fourier frequency satisfies $\rho_1^2 + \rho_2^2 > k^2$, the function $\hat{u}_s(\rho_1, \rho_2, z, \mathbf{x}_\alpha)$ decays exponentially with respect to $z \rightarrow -\infty$. Therefore, if the measurement surface is far away from the domain of interest, i.e. D is large, then we can neglect the term in the first line of (76). In other words, we can neglect high spatial frequencies in (76). Thus, we take $z = -D$ in (76) to get

$$\hat{\mathbf{U}}(\rho_1, \rho_2, \mathbf{x}_\alpha) = \hat{\mathbf{V}}(\rho_1, \rho_2, \mathbf{x}_\alpha) e^{i\sqrt{k^2 - \rho_1^2 - \rho_2^2}(-D+b)} \quad \text{for } \rho_1^2 + \rho_2^2 < k^2.$$

Using the inverse Fourier transform, we obtain

$$\begin{aligned} \mathbf{U}(x, y, \mathbf{x}_\alpha) &= u_s(x, y, -b, \mathbf{x}_\alpha) \\ &= \frac{1}{2\pi} \int_{\rho_1^2 + \rho_2^2 < k^2} \hat{\mathbf{V}}(\rho_1, \rho_2, \mathbf{x}_\alpha) e^{i\sqrt{k^2 - \rho_1^2 - \rho_2^2}D} e^{i(x\rho_1 + y\rho_2)} d\rho_1 d\rho_2 \\ &= \frac{1}{(2\pi)^2} \int_{\rho_1^2 + \rho_2^2 < k^2} \left[\int_{\mathbb{R}^2} u_s(\tilde{x}, \tilde{y}, -D, \mathbf{x}_\alpha) e^{-i(\tilde{x}\rho_1 + \tilde{y}\rho_2)} d\tilde{x} d\tilde{y} \right] e^{i\sqrt{k^2 - \rho_1^2 - \rho_2^2}(-D+b)} e^{i(x\rho_1 + y\rho_2)} d\rho_1 d\rho_2. \end{aligned} \quad (77)$$

The last formula of (77) is the actual data propagation procedure we will use in this work.

4.5. Computational setup

We introduce dimensionless variables as $\mathbf{x}' = \mathbf{x}/(10 \text{ cm})$ and keep the same notations as before, for brevity. This means that the dimensions we use in computations are 10 times less than the real ones in centimeters. We illustrate the choice of the coordinate system on Figures 2c, 3c, 4c, 5c and 6c: the x - and y -axis are horizontal and vertical sides respectively and z -axis is orthogonal to the measurement plane.

The far-field data are measured on a rectangular surface of dimensions $100 \text{ cm} \times 100 \text{ cm}$, i.e. 10×10 in dimensionless regime. Cf. Figure 1b as to our mesh grid of the measurement plane, each step is 2 cm (0.2) over 100 cm (10) length row. The total number of steps in a row is 50 , and the total number of steps in a column is also 50 . The distance between the measurement plane and the sandbox with the foam layer, whose thickness is 5 cm , is about 110.5 cm (11.05). The length in the z direction of the sandbox without the foam is approximately 44 cm , but due to the bending foam layer, we reduce 10% of this length. Henceforth, our choice of the domain Ω should be

$$\Omega = \{\mathbf{x} \in \mathbb{R}^3 : |x|, |y| < 5, |z| < 2\},$$

which implies that $R = 5$ and $b = 2$. The near-field or propagated measurement site is then assigned as

$$\Gamma := \{\mathbf{x} \in \mathbb{R}^3 : |x|, |y| < 5, z = -2\}.$$

Also, we take $D = 14$ for the far-field measurement site as we estimate the distance between this site and the zero point. Meanwhile, for all objects, for the line of sources L_{src} defined in section 2 we have $d = 9$, $a_1 = 0.1$ and $a_2 = 0.6$. Besides, we take $\theta = 4$.

It remains to obtain the wavenumber k corresponding to the dimensionless spatial variables we are working with. It is well-known that the relation between the wavelength ($\tilde{\lambda}$) and the wavenumber is expressed by $k = 2\pi/\tilde{\lambda}$. Basically, the wavelength can be computed via the formulation $\tilde{\lambda} = \tilde{v}/\tilde{f}$, where $\tilde{v} = 299792458 \text{ (m/s)}$ is the speed of light in vacuum and \tilde{f} is the frequency in Hertz (Hz or s^{-1}). Hence, in the computational setting we compute (in cm^{-1})

$$k = \frac{2\pi}{2997924580} \tilde{f}.$$

Example	1	2	3	4	5
k	8.51	6.62	11.43	9.55	8.79
Frequency (GHz)	4.06	3.16	5.45	4.55	4.19

Table 1: Wave numbers and frequencies for Examples 1–5.

The choice of k relies on the performance of the data after preprocessing. More precisely, our criterion is heuristically based upon the best visualization of the propagated data that we obtain using the data propagation. For each example below we then use its own frequency, which we specify in Table 1. Note that for each location of the detector we measure the backscatter data for 300 frequency points uniformly distributed between 1 GHz and 10 GHz.

Now, we summarize the crucial steps of the data preprocessing to obtain fine data for our inversion method from the raw ones.

- **Step 1.** For every frequency and for every location of the source, we subtract the reference data from the far-field measured data. A similar procedure was implemented in [30, 37]. The reference data are the background ones measured when the sandbox is without a target. This subtraction helps to extract the pure signals from buried objects from the whole signal. Therefore, we reduce the noise this way.
- **Step 2.** We apply the data propagation procedure as in subsection 4.4 to obtain the near-field data. This procedure provides a significantly better estimation for x, y coordinates of buried objects, and reduces the size of the computational domain in the z -direction.
- **Step 3.** We truncate the so obtained near-field data to get rid of random oscillations. The oscillations appear randomly during the data propagation and may cause unnecessary issues during our inversion procedure. This data truncation was developed in [37] and now we improve it using the following two steps, given a function $g(x, y, \alpha)$ to be truncated:

- For each point source, we replace the function $g(x, y, \alpha)$ with a function $\tilde{g}(x, y, \alpha)$ defined as:

$$\tilde{g}(x, y, \alpha) = \begin{cases} g(x, y, \alpha) & \text{if } |g(x, y, \alpha)| \geq \kappa_1 \max_{|x|, |y| \leq R} |g(x, y, \alpha)|, \\ 0 & \text{otherwise.} \end{cases}$$

Here, we call $\kappa_1 > 0$ the truncation number. Even though this number should be dependent of the source position α and should be different from every single choice of the frequency point, we apply the same truncation number to all the examples below. By the trial and error procedure, we have chosen $\kappa_1 = 0.4$, which means that we only preserve those propagated near-field data whose values are least 40 percents of the global maximum value.

- The next step would be smoothing the function \tilde{g} using the Gaussian filter. However, we notice that when doing so, the maximum value of \tilde{g} will be smaller than that of g . In order to preserve this important “peak” of g after truncation, we add back some percents of \tilde{g} in the following manner:

$$\tilde{g}_{\text{new}}(x, y, \alpha) = \kappa_2 \tilde{g}_{\text{old}}(x, y, \alpha). \quad (78)$$

Here, we call $\kappa_2 > 0$ the retrieval number. This number is computed by $\kappa_2 = \max(|\tilde{g}|) / \tilde{m}$, where \tilde{m} is the maximal absolute value of the smoothed \tilde{g}_{old} .

Fully discrete setting

We now present our numerical approach of the approximation of the right hand side of formula (77) in order to use it for our experimental data. First, we adapt the conventional Riemannian sum approximation to compute the Fourier transform of the function \mathbf{V} . Using (74) and the samples $\{u_s(\tilde{x}_i, \tilde{y}_j, -D, \mathbf{x}_\alpha)\}_{i,j=0}^{\tilde{N}-1}$ over a 2D finite domain, where we are experimentally measuring the far-field data, we find that

$$\hat{\mathbf{V}}(\rho_1, \rho_2, \mathbf{x}_\alpha) \approx \omega^2 \sum_{i,j=0}^{\tilde{N}-1} u_s(\tilde{x}_i, \tilde{y}_j, -D, \mathbf{x}_\alpha) \exp(-i(\tilde{x}_i \rho_1 + \tilde{y}_j \rho_2)).$$

Here, a uniform sampling rate, i.e. $\tilde{x}_i = i\Delta\tilde{x}_i, \tilde{y}_j = j\Delta\tilde{y}_j$, is used with $\Delta\tilde{x}_i = \Delta\tilde{y}_j = \omega$ for a number $\omega \in (0, 1)$.

Next, we define the following truncated Fourier domain in 2D:

$$\Theta_k := \{(\rho_1, \rho_2) \in \mathbb{R}^2 : \rho_1^2 + \rho_2^2 < k^2\}.$$

We sample this truncated Fourier domain at uniformly discrete points $\rho_{1m_1} = m_1\omega_\rho, \rho_{2m_2} = m_2\omega_\rho$ for a number $\omega_\rho \in (0, 1)$ and $0 \leq m_1, m_2 \leq \tilde{M} - 1$, provided that these points are in the set Θ_k . Thus, we conclude that

$$\begin{aligned} \mathbf{U}(x_p, y_q, \alpha_l) & \tag{79} \\ & \approx \frac{1}{(2\pi)^2} \omega_\rho^2 \sum_{m_1, m_2=0}^{\tilde{M}-1} \hat{\mathbf{V}}(\rho_{1m_1}, \rho_{2m_2}, \alpha_l) \exp\left(i\sqrt{k^2 - \rho_{1m_1}^2 - \rho_{2m_2}^2}(-D + b)\right) \exp\left(i(x_p \rho_{1m_1} + y_q \rho_{2m_2})\right). \end{aligned}$$

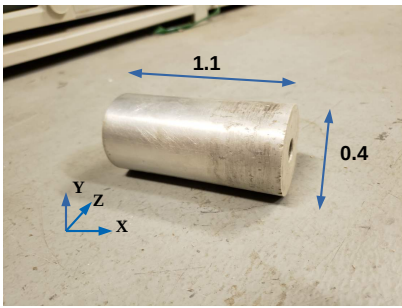
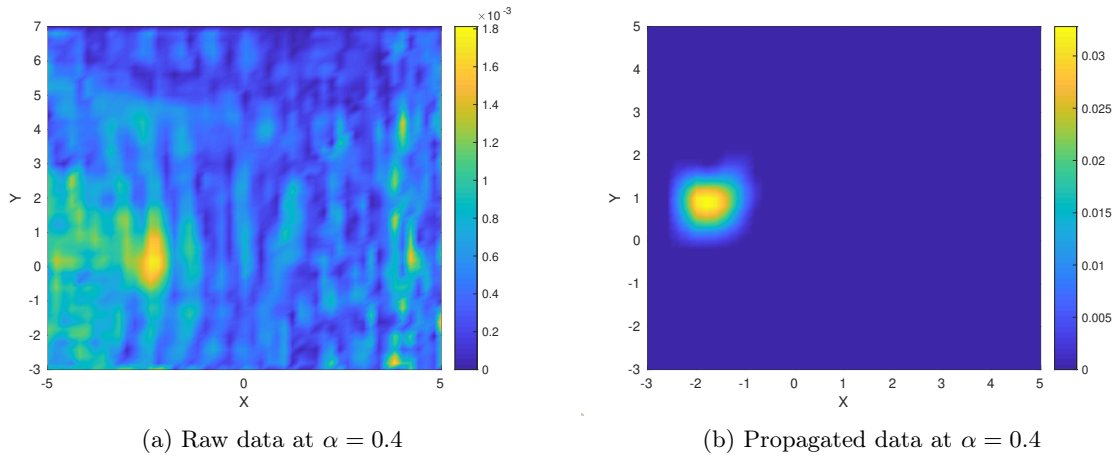
In our experimental data, we have $N_p = N_q = 51$, where N_p and N_q are the number of discrete points in x and y directions respectively. Therefore, we take $\tilde{N} = \tilde{M} = 51$, which gives $\omega = \omega_\rho = 1/50$. Thus, (79) gives us the approximate Dirichlet boundary condition $V(\mathbf{x}^h) = \psi_0^h(\mathbf{x}^h)$ at $\{z = -b\}$ in (49). Since we also need the function $V_z(\mathbf{x}^h) = \psi_1^h(\mathbf{x}^h)$ at $\{z = -b\}$ in (49), then to obtain it, we formally replace in (79) b with z , differentiate the right hand side of the obtained equality with respect to z , then set again $z := -b$ and calculate the resulting sum. The result is $\psi_1^h(\mathbf{x}^h)$ at $\{z = -b\}$ in (49).

Hence, the Cauchy boundary data in (49) are in the fully discrete form now. Then we write the functional $J_{h,\lambda}(V^h)$ defined in (24) in the fully discrete form, similarly to the semi-discrete form in (24). In this fully discrete setting we take into account the grid points in x, y, z directions, $\{(x_p, y_q, z_s)\}_{p,q,s=0}^{Z_h}$. For brevity, we do not bring in here this fully discrete form of $J_{h,\lambda}(V^h)$.

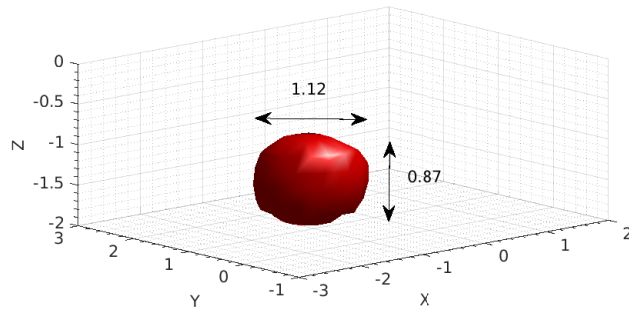
After the global minimum $V_{p,q,s}$ of the functional $J_{h,\lambda}(V^h)$ (in its discrete form) is obtained, we compute an approximation of the unknown dielectric constant $c_{p,q,s}$ using the following formula:

$$c_{p,q,s} = \text{mean}_{\alpha_l} \left| -\frac{\Delta^h v_{p,q,s,\alpha_l} + (\nabla^h v_{p,q,s,\alpha_l})^2 + 2\nabla^h v_{p,q,s,\alpha_l} \cdot \tilde{\mathbf{x}}_{p,q,s,\alpha_l}}{k^2} \right| + 1,$$

which is resulted from (10); see Remark 3. Here, $v_{p,q,s,\alpha_l} = v(x_p, y_q, z_s, \alpha_j)$. Recall that $\tilde{\mathbf{x}}_{p,q,s,\alpha_l}$ denote vectors $\tilde{\mathbf{x}}_\alpha$ at (x_p, y_q, z_s) for every α_l ; see subsection 3.1. Since the number of point sources is small, we apply the Gauss–Legendre quadrature method to compute the measured data in the Fourier mode. This was mentioned already in our previous work with simulated data; cf. [17].



(c) Aluminum cylinder

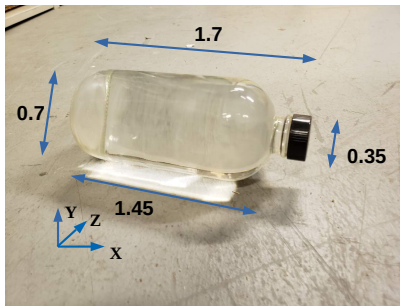
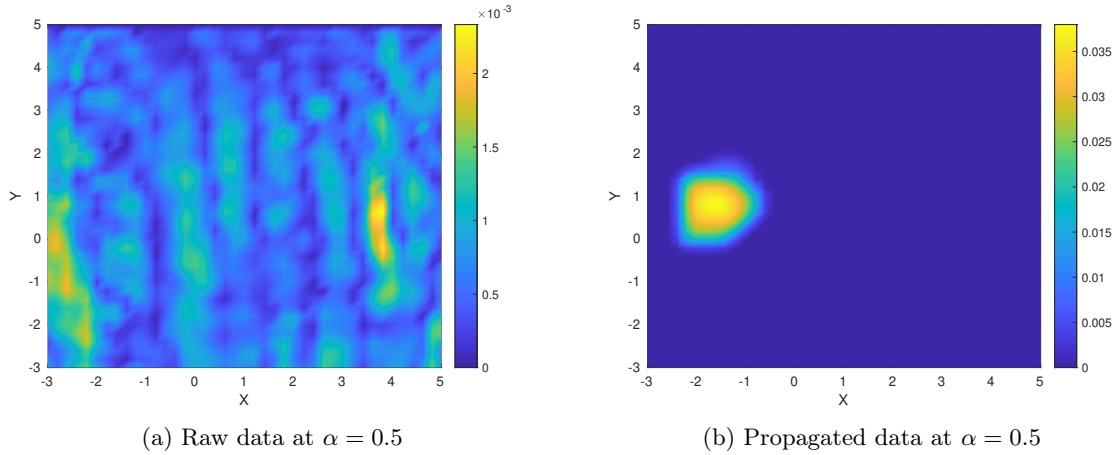


(d) Computed inclusion

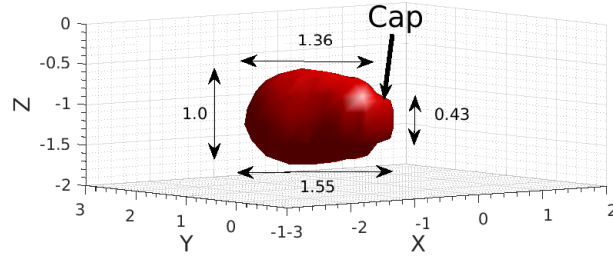
Figure 2: Reconstruction results of Test 1 (aluminum tube). (a) Illustration of the absolute value of the raw far-field data; (b) Illustration of the absolute value of the near-field data after the data propagation procedure; (c) Photo of the experimental object; (d) The computed image of (c). All images are in the dimensionless variables.

Since this work focuses on the detection and identification of antipersonnel land mines and IEDs, we know that the sizes of these targets are between 5 and 15 cm, cf. e.g. [37]. Therefore, we search for targets in a sub-domain of Ω with only 20 cm in depth in the z -direction. Denote this sub-domain by $\Omega_1 = \{-b \leq z \leq -b + 2\}$. We consider the following vector $V_0^h = V_0(x_p, y_q, z_s)$ as the starting point of iterations in the minimization of the functional $J_{\lambda, h}(V^h)$:

$$V_0^h = \left(v_{00}^h \quad v_{01}^h \quad \cdots \quad v_{0(N-1)}^h \right)^T, \quad v_{0n}^h = \left(\psi_{0n}^h + \psi_{1n}^h(z+b) \right) \chi(z). \quad (80)$$



(c) Glass bottle



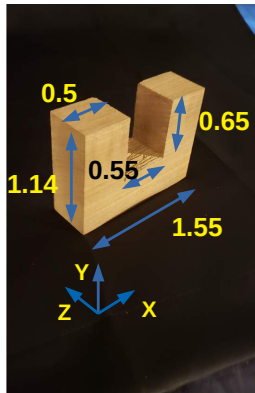
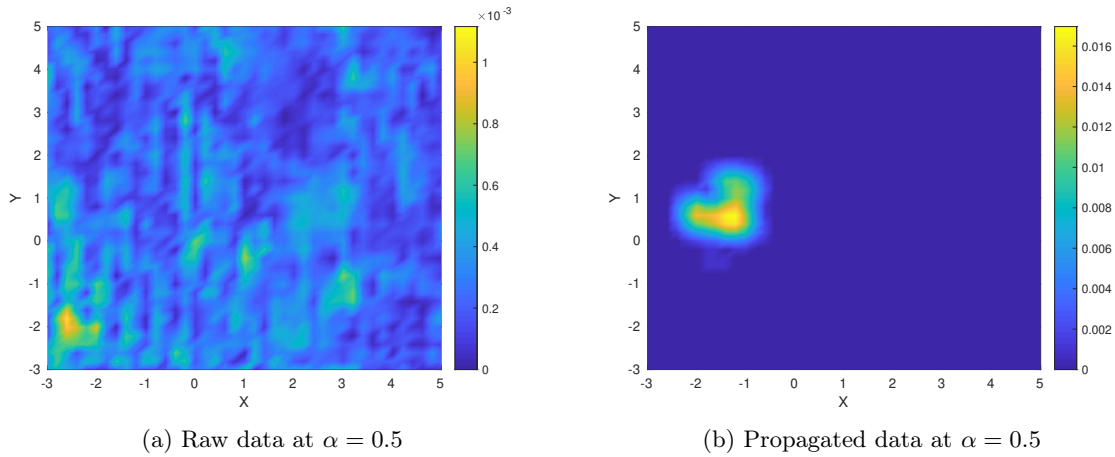
(d) Computed inclusion. Note that the cap of the bottle is clearly seen.

Figure 3: Reconstruction results of Test 2 (a glass bottle filled with clear water). (a) Illustration of the absolute value of the raw far-field data; (b) Illustration of the absolute value of the near-field data after the data propagation procedure; (c) Photo of the experimental object; (d) The computed image of (c). All images are in the dimensionless variables. An interesting point here is that we can even see the cap of the bottle in (d), which is challenging to image.

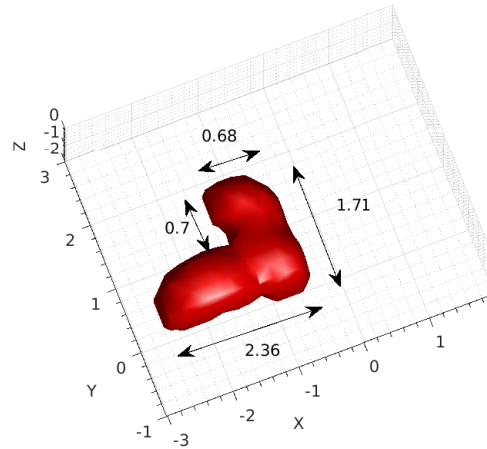
Recall that ψ_{0n}^h and ψ_{1n}^h are the Fourier coefficients of the propagated data in (49). Here, $\chi : [-b, b] \rightarrow \mathbb{R}$ is the smooth function given by

$$\chi(z) = \begin{cases} \exp\left(\frac{2(z+b)^2}{(z+b)^2 - b^2}\right) & \text{if } z < 0, \\ 0 & \text{otherwise.} \end{cases}$$

This function attains the maximum value 1 at $z = -b$ where the propagated data are given. Then, it is easy to see that $v_{0n}^h|_{z=-b} = \psi_{0n}^h$, $\partial_z v_{0n}^h|_{z=-b} = \psi_{1n}^h$. On the other hand, χ tends to 0 as $z \rightarrow 0^+$, which, in particular, means that $v_{0n}^h|_{z=b} = \partial_z v_{0n}^h|_{z=b} = 0$. Thus, this starting point (80) of iterations satisfies the boundary conditions (49).



(c) U-shaped piece of dry wood



(d) Computed inclusion

Figure 4: Reconstruction results of Test 3 (U-shaped piece of dry wood). Note that the shape is non-convex, which is difficult to image. (a) Illustration of the absolute value of the raw far-field data; (b) Illustration of the absolute value of the near-field data after the data propagation procedure; (c) Photo of the experimental object; (d) The computed image of (c). Note that the void is clearly seen which is difficult to image. Our axes on (d) are oriented differently from ones on (c) due to some technical problem of the imaging software. These axes are comparable. All images are in the dimensionless variables.

Although Theorem 7 claims the global convergence of the gradient projection method, we have successfully used the gradient descent method for the minimization of the target functional $J_{h,\lambda}(V^h)$ of (24). Clearly, the gradient descent method is easier to implement than the gradient projection method. Our success in working with the gradient descent method is similar with the success in all previous publications discussing the numerical studies of the convexification [17, 27, 28, 29, 30, 31, 32]. As to the value of the parameter λ in $J_{h,\lambda}(V^h)$, even though the analysis requires large values of λ , our numerical experience

Example number	1	2	3	4	5
Object	Metal Cylinder	Water	Wood	Metal letter “A”	Metal letter “O”
$\max(c_{\text{comp}})$	18.72	23.29	6.56	15.01	16.25
c_{true}	[10,30]	23.8	[2, 6]	[10,30]	[10,30]
Reference	[35]	[44]	[43]	[35]	[35]

Table 2: True c_{true} and computed $\max(c_{\text{comp}})$ dielectric constants of Examples 1–5 of experimental data. True values were taken from: (a) Examples 1, 4, 5: formula (7.2) of [35], (b) Example 2 (clear water) [44], (c) Example 3 [43].

tells us that we can choose a moderate value of λ :

$$\lambda = 1.1.$$

Again similar values of $\lambda \in [1, 3]$ were chosen in the above cited publications on the convexification.

As to the step size γ of the gradient descent method, we start from $\gamma_1 = 10^{-1}$. For each iteration step $m \geq 1$, the following step size γ_m is reduced by the factor of 2 if the value of the functional on the step m exceeds its value of the previous step. Otherwise, $\gamma_{m+1} = \gamma_m$. The minimization process is stopped when either $\gamma_m < 10^{-10}$ or $|J_{h,\lambda}(V_m^h) - J_{h,\lambda}(V_{m-1}^h)| < 10^{-10}$. As to the gradient $J'_{h,\lambda}$ of the discrete functional $J_{h,\lambda}$, we apply the technique of Kronecker deltas (cf. e.g. [34]) to derive its explicit formula, which significantly reduces the computational time. For brevity, we do not provide this formula here.

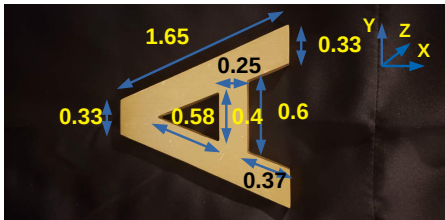
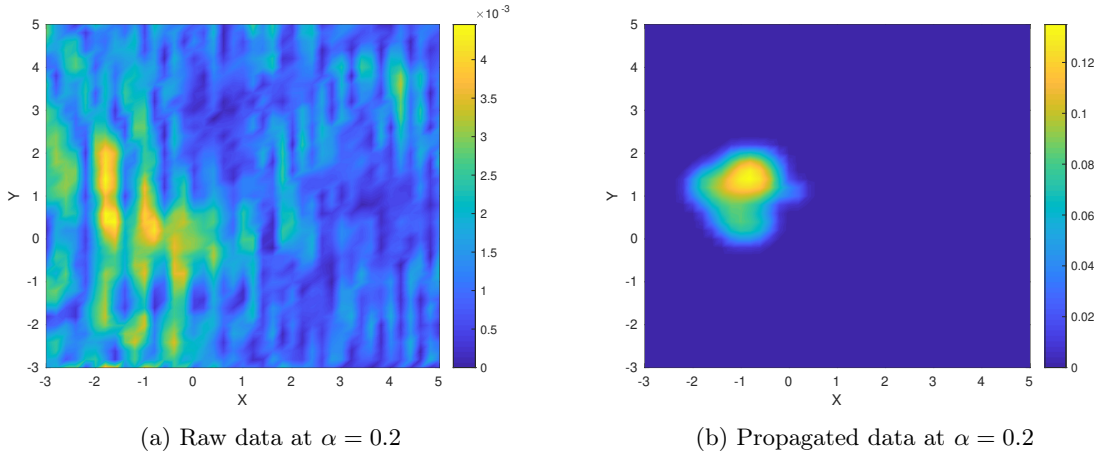
After the minimization procedure is stopped, we obtain numerically the coefficient of $c_{p,q,s}$, denoted by \tilde{c} . Our reconstructed solution, denoted by c_{comp} , is concluded after we smooth \tilde{c} by the standard filtering via the `smooth3` built-in function in MATLAB. In fact, we find c_{comp} by using $c_{\text{comp}} = \hat{\varrho}\text{smooth}(|\tilde{c}|)$, for some $\hat{\varrho} > 0$ depending on every single example. This step is definitely similar to the smoothing procedure discussed in (78) and we do not repeat how to find $\hat{\varrho}$ here. We use this step to get better images.

4.6. Reconstruction results

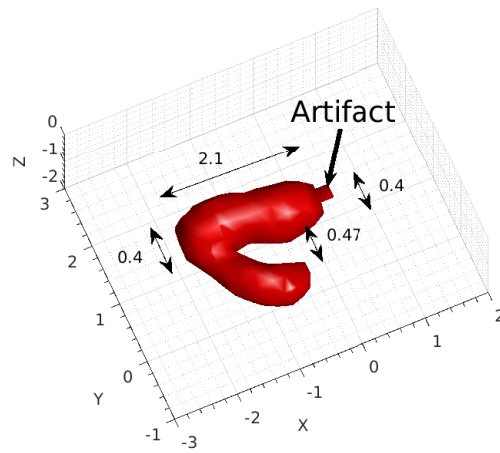
Values of $\max(c_{\text{true}})$ and $\max(c_{\text{comp}})$ for all five tests are tabulated in Table 2. Values of $\max(c_{\text{true}})$ for all tests are mentioned in subsection 4.2, which were used, are published ones [35, 43, 44]. More precisely, as to the metallic targets of Example 1 (aluminum cylinder), Example 4 (metallic letter “A”) and Example 5 (metallic letter “O”), it was numerically established that one can treat metals as materials with large values of the dielectric constant in the interval $c \in [10, 30]$, see the formula (7.2) of [35]. As to the Example 2, the dielectric constant of the clear water for our frequency range was directly measured in [44], and it was 23.8: see the first line of Table 2 of [44]. As to the Example 3 (an U-shaped piece of a dry wood), the table of dielectric constants [43] tells one that in the dielectric constant of a dry wood is $c \in [2, 6]$.

Figures 2a, 3a, 4a, 5a and 6a show how “bad” the far-field data look like. It is clear from these figures that something should be done to the data to have a proper inversion. On the other hand, one can see the good shapes of the corresponding images after the data propagation procedure; see Figures 2b, 3b, 4b, 5b and 6b. For every test, we deliberately show the 2D illustrations (raw and propagated) of the data at a specific point source, where the images of the propagated data and the computed inclusion are congruent with each other.

3D images of computed inclusions are depicted by using the `isosurface` function in MATLAB with the associated `isovalue` being 10% of the maximal value; see Figures 2d, 3d, 4d, 5d and 6d. The most challenging targets to image were: (1) The U-shaped piece of dry wood, see Figure 4, (2) The metallic letter “A”, see Figure 5, and (3) the metallic letter “O”, see Figure 6. This is because these targets have the most complicated geometries. Nevertheless, we are still able to see their characteristic shapes in the images of computed inclusion.



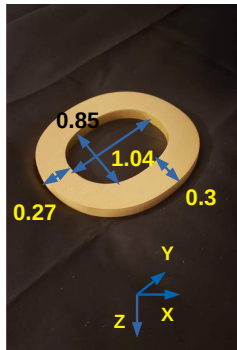
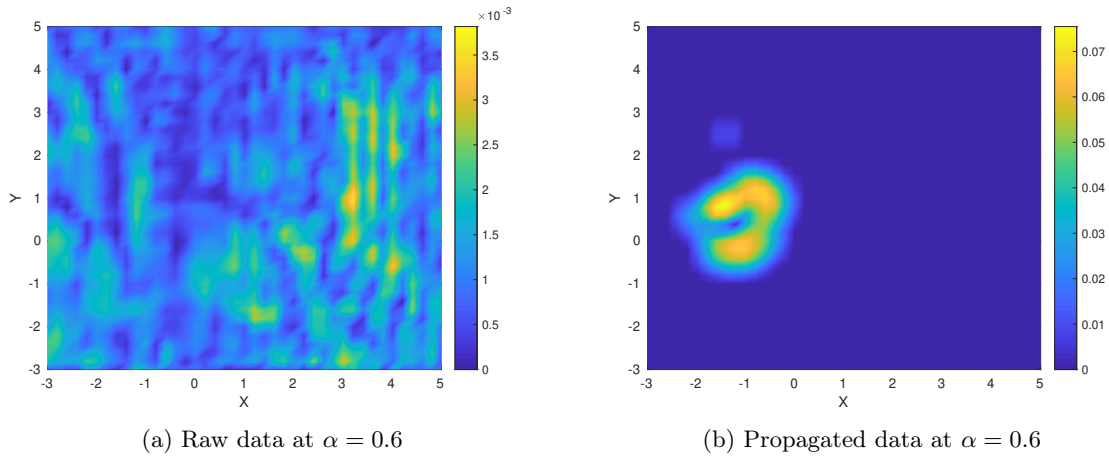
(c) Metallic letter “A”. Blind test. The shape is non-convex, which is difficult to image.



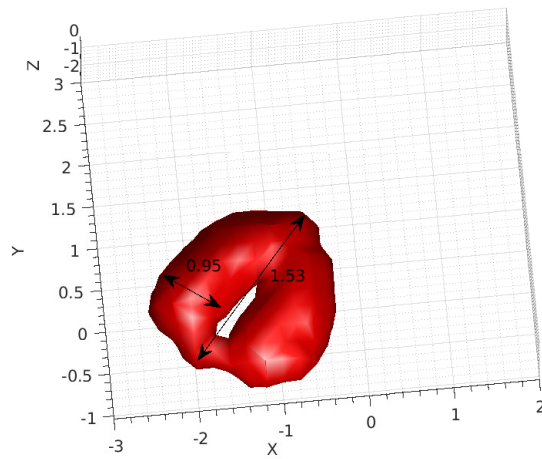
(d) Computed inclusion

Figure 5: Reconstruction results of Test 4 (metallic letter “A”). This is a blind test. (a) Illustration of the absolute value of the raw far-field data; (b) Illustration of the absolute value of the near-field data after the data propagation procedure; (d) The computed image of (c). Note that the void is clearly seen, which is challenging to image. Also, sizes of the imaged target are close to the true ones. The strip of “A” is not seen since its width is 2.5 cm, which is less than the wavelength of 10.4 cm we have used with $k = 9.55$. All images are in the dimensionless variables.

Most notably, one can see voids in imaged letters “A” and “O”. The latter is usually difficult to achieve. The “strip” of the letter “A” is not imaged since its width was 2.5 cm, which is less than the used wavelength of 10.4 cm with $k = 9.55$. Another interesting observation is that we can even see the cap on the bottle of water on Figure 3d.



(c) Metallic letter “O”. Blind test. The shape is non-convex, which is challenging to image.



(d) Computed inclusion

Figure 6: Reconstruction results of Test 5 (metallic letter “O”). This is a blind test. (a) Illustration of the absolute value of the raw far-field data; (b) Illustration of the absolute value of the near-field data after the data propagation procedure; (c) Photo of the experimental object; (d) The computed image of (c). Note that the void is clearly seen, which is not easy to image. All images are in the dimensionless variables.

We also find that the lengths of parts of true and computed inclusions are quite compatible with each others. Note that even though the computed inclusions here are slightly larger (just a few centimeters) than the true ones, it is still useful in detection and identification of land mines and further in the mine-clearing operations. In fact, having information of smaller sizes is rather dangerous. Hence, we conclude that the dimensions of the computed inclusions are acceptable.

Finally, we can accurately obtain approximations of the dielectric constants. Aside from the dielectric constant of metallic targets, we notice from Table 2 that the relative errors obtained for the bottle with water and for the wooden target are 2.14% and 9.33%, respectively.

5. Summary

We have developed a new version of the globally convergent convexification method for the case of a 3D CIP for the Helmholtz equation. In our case, the point source is moving along an interval of a straight line and the frequency is fixed. For each position of the point source we measure one component of the backscattering electric wave field at a part of a plane. Thus, our data depend on three variables, which means that they are non overdetermined ones. We use the partial finite differences and construct a weighted cost functional with the Carleman Weight Function in it. The use of partial finite differences enables us to avoid the use of the penalty regularization term. The latter is the major analytical novelty here. We prove that our functional is strictly convex on a finite set of an arbitrary size. This theorem leads to the theorem about the *global convergence* to the exact solution of the gradient projection method of the minimization of this functional, as long as the level of noise in the data tends to zero. The global convergence property is the most important feature of the convexification method.

We have tested our method numerically on backscattering experimentally collected data. Our testing reveals that we can accurately image both dielectric constants and shapes of targets of interest. Including even rather complicated geometries. This is an advantage compared with the previously considered version of the convexification in which the point source was fixed and the frequency was varied. Indeed, while in the latter case the dielectric constants were computed accurately, shapes were not accurately imaged; see, e.g., [30] for the case of experimental data.

References

- [1] A. D. Agaltsov, T. Hohage and R. G. Novikov, An iterative approach to monochromatic phaseless inverse scattering, *Inverse Problems*, 35 (2019), 24001, 2019.
- [2] N. V. Alekseenko, V. A. Burov and O. D. Rumyantseva, Solution of the three-dimensional acoustical inverse scattering problem. The modified Novikov algorithm, *Acoustical Physics*, 54 (2008), 407–419.
- [3] A. B. Bakushinskii, M. V. Klibanov and N. A. Koshev, Carleman weight functions for a globally convergent numerical method for ill-posed Cauchy problems for some quasilinear PDEs, *Nonlinear Analysis: Real World Applications*, 34 (2017), 201–224.
- [4] A. B. Bakushinsky and A. S. Leonov, To the numerical solution of the inverse multi-frequency scalar acoustics problem, (2019), preprint at arXiv:1911.10487v1.
- [5] E. Banks, *Anti-Personnel Landmines: Recognising & Disarming (Brassey’s Essential Guides)*, Potomac Books Inc, 1998.
- [6] L. Baudouin, M. de Buhan and S. Ervedoza, Convergent algorithm based on Carleman estimates for the recovery of a potential in the wave equation, *SIAM Journal on Numerical Analysis*, 55 (2017), 1578–1613.
- [7] L. Baudouin, M. de Buhan, S. Ervedoza and A. Osses, Carleman-based reconstruction algorithm for the waves, (2020), preprint at <https://hal.archives-ouvertes.fr/hal-02458787>.
- [8] L. Beilina and M. V. Klibanov, *Approximate Global Convergence and Adaptivity for Coefficient Inverse Problems*, Springer US, 2012.
- [9] L. Beilina, M. V. Klibanov, Globally strongly convex cost functional for a coefficient inverse problem, *Nonlinear Analysis: Real World Applications*, 22 (2015), 272–288.

- [10] M. Boulakia, M. de Buhan and E. L. Schwindt, Numerical reconstruction based on Carleman estimates of a source term in a reaction-diffusion equation, (2019), preprint at <https://hal.archives-ouvertes.fr/hal-02185889>.
- [11] A. L. Bukhgeim and M. V. Klibanov, Global uniqueness of a class of multidimensional inverse problems, *Doklady Akademii Nauk SSSR*, 260 (2) (1981), 269–272. English translation: *Soviet Mathematics Doklady*, 24 (2) (1981), 244–247.
- [12] G. Chavent, *Nonlinear Least Squares for Inverse Problems—Theoretical Foundations and Step-by-Step Guide for Applications*, Springer, New York, 2009.
- [13] A. V. Goncharsky and S. Y. Romanov, A method of solving the coefficient inverse problems of wave tomography, *Computers and Mathematics with Applications*, 77 (2019), 967–980.
- [14] A. V. Goncharsky, S. Y. Romanov and S. Y. Seryozhnikov, Low-frequency ultrasonic tomography: mathematical methods and experimental results, *Moscow University Physics Bulletin*, 74 (1) (2019), 43–51.
- [15] S. I. Kabanikhin, K. K. Sabelfeld, N. S. Novikov and M. A. Shishlenin, Numerical solution of the multidimensional Gelfand–Levitan equation, *Journal of Inverse and Ill-Posed Problems*, 23 (2015), 439–450.
- [16] S. I. Kabanikhin, N. S. Novikov, I. V. Osedelets and M. A. Shishlenin, Fast Toeplitz linear system inversion for solving two-dimensional acoustic inverse problem, *Journal of Inverse and Ill-Posed Problems*, 23 (2015), 687–700.
- [17] V. A. Khoa, M. V. Klibanov and L. H. Nguyen, Convexification for a 3D inverse scattering problem with the moving point source, to appear in *SIAM Journal on Imaging Sciences*, (2020), preprint at [arXiv:1911.10289v2](https://arxiv.org/abs/1911.10289v2).
- [18] M. V. Klibanov and O. Ioussoupova, Uniform strict convexity of a cost functional for three-dimensional inverse scattering problem, *SIAM Journal on Applied Mathematics*, 26 (1995), 147–179.
- [19] M. V. Klibanov, Global convexity in a three-dimensional inverse acoustic problem, *SIAM Journal on Mathematical Analysis*, 28 (1997), 1371–1388.
- [20] M. V. Klibanov and A. Timonov, *Carleman Estimates for Coefficient Inverse Problems and Numerical Applications*, VSP, Utrecht, 2004. Second edition: de Gruyter, 2012.
- [21] M. V. Klibanov, Carleman estimates for global uniqueness, stability and numerical methods for coefficient inverse problems, *Journal of Inverse and Ill-posed Problems*, 21 (4) (2013).
- [22] M. V. Klibanov, V. G. Kamburg, Globally strictly convex cost functional for an inverse parabolic problem, *Mathematical Methods in the Applied Sciences*, 39 (2015), 930–940.
- [23] M. V. Klibanov, Carleman estimates for the regularization of ill-posed Cauchy problems, *Applied Numerical Mathematics*, 94 (2015), 46–74.
- [24] M. V. Klibanov, L. H. Nguyen, A. Sullivan and L. Nguyen, A globally convergent numerical method for a 1-d inverse medium problem with experimental data, *Inverse Problems and Imaging*, 10 (2016), 1057–1085.
- [25] M. V. Klibanov and V. G. Romanov, Reconstruction procedures for two inverse scattering problems without the phase information, *SIAM Journal on Applied Mathematics*, 76 (2016), 198–196.

- [26] M. V. Klibanov, Convexification of restricted Dirichlet-to-Neumann map, *Journal of Inverse and Ill-posed Problems*, 25 (2017), 669–685.
- [27] M. V. Klibanov, A. E. Kolesov and L. Nguyen and A. Sullivan, Globally strictly convex cost functional for a 1-D inverse medium scattering problem with experimental data, *SIAM Journal on Applied Mathematics*, 77 (5) (2017), 1733–1755.
- [28] M. V. Klibanov, A. E. Kolesov, L. Nguyen and A. Sullivan, A new version of the convexification method for a 1D coefficient inverse problem with experimental data, *Inverse Problems*, 34 (2018), 35005.
- [29] M. V. Klibanov and A. E. Kolesov, Convexification of a 3-D coefficient inverse scattering problem, *Computers & Mathematics with Applications*, 77 (6) (2019), 1681–1702.
- [30] M. V. Klibanov and A. E. Kolesov and D. -L. Nguyen, Convexification method for an inverse scattering problem and its performance for experimental backscatter data for buried targets, *SIAM Journal on Imaging Sciences*, 12 (1) (2019), 576–603.
- [31] M. V. Klibanov, J. Li and W. Zhang, Convexification of electrical impedance tomography with restricted Dirichlet-to-Neumann map data, *Inverse Problems*, 35 (3) (2019), 035005.
- [32] M. V. Klibanov, J. Li and W. Zhang, Convexification for the inversion of a time dependent wave front in a heterogeneous medium, *SIAM Journal on Applied Mathematics*, 79 (2019), 1722–1747.
- [33] M. V. Klibanov, D. -L. Nguyen and L. H. Nguyen, A coefficient inverse problem with a single measurement of phaseless scattering data, *SIAM Journal on Applied Mathematics*, 79 (2019), 1–47.
- [34] A. V. Kuzhuget and M. V. Klibanov, Global convergence for a 1-D inverse problem with application to imaging of land mines, *Applicable Analysis*, 89 (2010), 125–157.
- [35] A. V. Kuzhuget, L. Beilina, M. V. Klibanov, A. Sullivan, L. Nguyen and M. A. Fiddy, Blind backscattering experimental data collected in the field and an approximately globally convergent inverse algorithm, *Inverse Problem*, 28 (2012), 095007.
- [36] T. T. Le and L. H. Nguyen, A convergent numerical method to recover the initial condition of nonlinear parabolic equations from lateral Cauchy data, (2019), preprint at arXiv: 1910.05584.
- [37] D. -L. Nguyen, M. V. Klibanov, L. H. Nguyen and M. A. Fiddy, Imaging of buried objects from multi-frequency experimental data using a globally convergent inversion method, *Journal of Inverse and Ill-posed Problems*, 26 (4) (2018), 501–522.
- [38] H. T. Nguyen, V. A. Khoa and V. A. Vo, Analysis of a quasi-reversibility method for a terminal value quasi-linear parabolic problem with measurements, *SIAM Journal on Mathematical Analysis*, 51 (1) (2019), 60–85.
- [39] R. G. Novikov, Multidimensional inverse spectral problem for the equation $-\Delta\psi + (v(x) - Eu(x))\psi = 0$, *Functional Analysis and Applications*, 22 (4) (1988), 263–272.
- [40] R. G. Novikov, The $\bar{\partial}$ -bar approach to approximate inverse scattering at fixed energy in three dimensions, *International Mathematical Research Papers*, 2005:6 (2005), 287–349.
- [41] R. G. Novikov, An iterative approach to non-overdetermined inverse scattering at fixed energy, *Sbornik: Mathematics*, 206 (2015), 120–134.

- [42] Office of the Chief of Ordnance, Catalog of enemy ordnance materiel. In: World War II Operational Documents, N2228-E, OCLC 464601649, 1945.
- [43] Clipper Controls Inc. (n.d.) Dielectric Constants of various materials. <http://www.clippercontrols.com/pages/Dielectric-Constant-Values.html#W>
- [44] N. T. Thành, L. Beilina, M. V. Klibanov and M. A. Fiddy, Imaging of buried objects from experimental backscattering time-dependent measurements using a globally convergent inverse algorithm, *SIAM Journal on Imaging Sciences*, 8 (1) (2015), 757–786.
- [45] A. N. Tikhonov, A. V. Goncharsky, V. V. Stepanov and A. G. Yagola, *Numerical Methods for the Solution of Ill-Posed Problems*, Springer Netherlands, 1995.
- [46] T. Truong, D. -L. Nguyen and M. V. Klibanov, Convexification numerical algorithm for a 2D inverse scattering problem with backscatter data, (2020), preprint at arXiv: 2002.08427v2.
- [47] M. Yamamoto, Uniqueness and stability in multidimensional hyperbolic inverse problems, *Journal de Mathématiques Pures et Appliquées*, 78 (1) (1999), 65–98.